

Cooperative Multi-Point Vehicular Positioning Using Millimeter-Wave Surface Reflection

Zezhong Zhang, Seung-Woo Ko, Rui Wang, and Kaibin Huang

Abstract

Multi-point vehicular positioning is one essential operation for autonomous vehicles. However, the state-of-the-art positioning technologies, relying on reflected signals from a target (i.e., RADAR and LIDAR), cannot work without *line-of-sight* (LoS). Besides, it takes significant time for environment scanning and object recognition with potential detection inaccuracy, especially in complex urban situations. Some recent fatal accidents involving autonomous vehicles further expose such limitations. In this paper, we aim at overcoming these limitations by proposing a novel relative positioning approach, called *Cooperative Multi-point Positioning* (COMPOP). The COMPOP establishes cooperation between a *target vehicle* (TV) and a *sensing vehicle* (SV) if a LoS path exists, where a TV explicitly lets an SV to know the TV's existence by transmitting positioning waveforms. This cooperation makes it possible to remove the time-consuming scanning and target recognizing processes, facilitating real-time positioning. One prerequisite for the cooperation is a clock synchronization between a pair of TV and SV. To this end, we use a *phase-differential-of-arrival* (PDoA) based approach to remove the TV-SV clock difference from the received signal. With clock difference correction, the TV's position can be obtained via peak detection over a 3D power spectrum constructed by a *Fourier transform* (FT) based algorithm. The COMPOP also incorporates nearby vehicles, without knowing their locations, into the above cooperation for the case without a LoS path. Specifically, several strong *non-LoS* (NLoS) links from the TV to the SV can be generated via mirror-like reflections over the neighboring vehicles' metal surfaces. Following procedures in the LoS case, virtual TVs mirrored by nearby vehicles can be detected. By exploiting the geometric relation between the virtual and actual TVs, COMPOP can be achieved by intelligently combining the virtual TVs to position the actual TV. The effectiveness of the COMPOP is verified by several simulations concerning practical channel parameters.

Ze Zhong Zhang and Kaibin Huang are with The University of Hong Kong, Hong Kong (Email: {zzzhang, huangkb}@eee.hku.hk). Seung-Woo Ko is with Korea Maritime and Ocean University, Korea (email: swko@kmou.ac.kr). Rui Wang is with Southern University of Science and Technology, China (Email: wang.r@sustech.edu.cn). Part of this work was presented in IEEE GLOBECOM 2019 [1].

I. INTRODUCTION

Vehicular positioning is one of the most important operations for autonomous driving and a challenging one as it requires high accuracy and low latency [2], [3]. Presently, for long-range positioning (e.g., hundreds of meters), a *target vehicle* (TV) is abstracted as a single point, and its GPS location is communicated to the *sensing vehicle* (SV) over either a vehicle-to-vehicle link or across a wireless network [4], [5]. For medium to short-range positioning (tens to several meters), the single-point abstraction of the TV no longer suffices, and its geometric information (e.g., size and orientation) is also required for safe and accurate driving. In these ranges, the popular positioning technologies include *RA*dio-*DE*tectio*N*-*AN*d-*R*ang*ING* (RADAR) and *LI*ght-*DE*tectio*N*-*AN*d-*R*ang*ING* (LIDAR). They face the challenges of long computation latency caused by complex signal processing and computer vision, potential inaccuracy of identifying TVs from their background environments, and ineffectiveness in the presence of blockages between a TV-SV pair. Their drawbacks have contributed to many accidents involving self-driving cars. To overcome these limitations of current technologies, we present in this paper a new technology for relative positioning at the SV, called *Cooperative Multi-point Positioning* (COMPOP). Essentially, by detecting the cooperative signals broadcast by multi-antennas distributed at a TV, the SV estimates the antenna positions representing the TV skeleton, thereby performing multi-point TV positioning. Algorithms based on *Fourier transform* (FT) are proposed for fast and accurate COMPOP not only when there are *lines-of-sight* (LoS) but also when they are blocked. The latter exploits the signals reflected by the surfaces of nearby vehicles.

A. Single-Point Positioning

Single-point positioning techniques were originally developed for locating mobile devices and recently also applied to autonomous driving. The most popular and simplest is to use a built-in *Global Positioning System* (GPS) receiver for computing the receiver's position and sharing the information to peer devices over wireless links. However, in an urban environment, the required LoS links between GPS receivers and satellites are often blocked by e.g., buildings or tunnels. This issue has motivated researchers to develop alternative techniques relying on base stations or access points in wireless networks as anchors to estimate the position of a mobile by either triangularization or measuring signal power [6]. This requires the mobile to estimate anchors' positions from their signals. The negative effect of mobility on estimation accuracy can be coped with by utilizing sampled temporal measurements and motion models [5].

Nevertheless, due to the unreliability of fading channels, such positioning techniques assisted by a wireless network cannot reach the level of precision required for autonomous driving. The required high-resolution positioning can be realized by *ultra-wideband* (UWB) radios leveraging the fact that a large bandwidth overcomes multi-path fading and thereby enables accurate *time-of-arrival* (ToA) measurements [7]. To avoid the need of transmitter-receiver clock synchronization, *time-difference-of-arrival* (TDoA) and *phase-difference-of-arrival* (PDoA) based methods are proposed which cancel at a receiver the clock difference of a transmitter (anchor) by observing received signals from different antennas or frequencies [8], [9]. Most recently, TDoA-based positioning over *non-LoS* (NLoS) links is made possible by separating multi-paths and locating the source via exploiting the paths' geometric relation [10]. The deployment of such techniques enables the positioning of a hidden TV (one without an LoS link). Despite having a rich literature, the outputs of single-point positioning are insufficient for complex maneuvers in autonomous driving such as platooning and overtaking, for which multi-point TV positioning is required.

B. Vehicular Sensing

Vehicular sensing can be treated as an extreme form of multi-point positioning. The sensing process involves scanning the surrounding environment and then recognizing, imaging, and positioning objects useful for autonomous driving (such as nearby pedestrians and vehicles). Usually vehicular sensing does not rely on the GPS link, which detects relative locations of objects independently with an on-board sensing system. Relevant technologies can be grouped as passive or active, depending on whether they require radiation. Typical passive sensors include infrared sensors, cameras, and passive *millimeter waves* (mmWave) sensors. They exploit ambient and unintended infrared radiation, light, and mmWave to image the sources and reflectors [11]. The two most popular types of active vehicular sensors are RADAR and LIDAR [2], [12]. A RADAR scans the environment by steering a microwave beam using an antenna array and observes reflected signals with varying attenuation to image the environment [13]–[15]. Subsequently, targeted objects are detected and positioned using signal processing and computer vision. LIDAR operates based on a similar principle except for replacing the microwave beam with a mechanically steered sharp laser beams, thereby achieving a higher resolution [16]. Among the sensing technologies, those based on light (i.e., cameras) or infrared (e.g., infrared sensors) are exposed to severe performance degradation caused by hostile weather such as heavy rains and

thick fogs [17]. Overall, existing multi-point positioning technologies share two drawbacks that present key challenges for vehicular sensing and positioning, as described below.

- **Latency and accuracy:** Environmental scanning (for RADAR and LIDAR) and object recognition (for RADAR, LIDAR, and cameras) are time-consuming. For example, a 3D beam scanning by a RADAR using a large-scale phased array can incur around ten-second latency [15]. This is unacceptable for autonomous driving in a crowded urban environment or at high speeds. On the other hand, objective recognition using a well-trained deep neural network with an onboard GPU typically takes several seconds. Furthermore, existing objective recognition techniques relying on offline training are easily affected by a variation on object features. As a result, the detection accuracy is usually in the range of 70% \sim 90% [18]. Their application to auto-driving presents safety threats, as exemplified by recent fatal accidents.
- **Hidden vehicle detection:** Besides TVs in sight, detecting hidden vehicles in the sensing blind spots (e.g., a TV around a street corner) can avoid many potential accidents. Though some progress has been made on NLoS single-point TV positioning, the desired detection of hidden TVs as multi-point objects is still an uncharted area and the theme of this work.

C. Main Contributions

Multi-point TV positioning refers to positioning a TV as a multi-point object where each point corresponds to a transmit antenna. As an attempt to tackle the two challenges discussed in the preceding section, we propose in this work the framework of *cooperative multi-point positioning* (COMPOP) at a SV building on the cooperation that a TV broadcasts a signal with a waveform that facilitates relative TV positioning at the SV. In this framework, latency reduction is achieved in two ways.

- The first is to retrieve from the total received signal the desired TV signal for further processing using the embedded signature. This avoids the time-consuming conventional method of environmental scanning and learning-based TV identification.
- The second is to apply the low-latency FT to efficiently compute a power spectrum distributed over the 3D space. This allows direct positioning by peak detection.

To tackle the second challenge of multi-point positioning without an LoS link, we propose a novel technique of using reflected TV signals over the smooth surfaces of nearby vehicles to position multiple “virtual TVs”. Then we exploit their geometry for combining to position the actual TV without any priori knowledge of the nearby vehicles. By overcoming these two key

challenges to the existing positioning approaches, we believe that the proposed technique can be well integrated with the current positioning system for improving the safety of autonomous driving.

The specific designs of the proposed COMPOP framework are summarized as follows.

- **COMPOP over a LoS link:** The framework for this case comprises two key algorithms operating in separate bandwidths. First, due to transceiver separation, clock synchronization between the transceivers are necessary for coherent signal demodulation at the SV. By using two reserved single tones and given the knowledge of TV signature waveform, we propose to use a PDoA-based iterative algorithm for TV-SV synchronization by accurately estimating their clock difference from the received TV signals in the presence of channel noise. Second, the remaining bandwidth is used by the TV to transmit a conventional *stepped-frequency-continuous-wave* (SFCW), a multi-tone waveform with a uniform frequency gap between tones [13]. After correcting the clock difference, a determined relation between the TV position and the received SFCW signal is established. As a main feature of COMPOP, we propose the application of FT to transform the received SFCW signal into the mentioned spectrum over the 3D space for estimating the TV position by peak detection. Besides, the positioning accuracy is analyzed.
- **COMPOP over mirror-reflection links:** For the case without LoS, but with nearby vehicles as reflectors, a COMPOP technique is developed as follows. The combined use of antenna array and TV signature allows the SV to resolve the received signals as reflected by different smooth vehicular surfaces. The application of the preceding technique for LoS COMPOP on the resolved signals yields multi-point positions of multiple “virtual vehicles”. Without priori knowledge of the nearby vehicles’ locations, an intelligent combining approach is proposed to position the actual TV by exploiting the geometric relation between the virtual and actual TVs.

The remainder of this paper is organized as follows. In Section II, the system model and signal model are introduced. In Section III and IV, the proposed COMPOP is elaborated and analyzed in both LoS and NLoS conditions, and a systematic comparison between the proposed and existing techniques is presented. The realistic simulation results are presented in Section V, and the conclusion follows in Section VI.

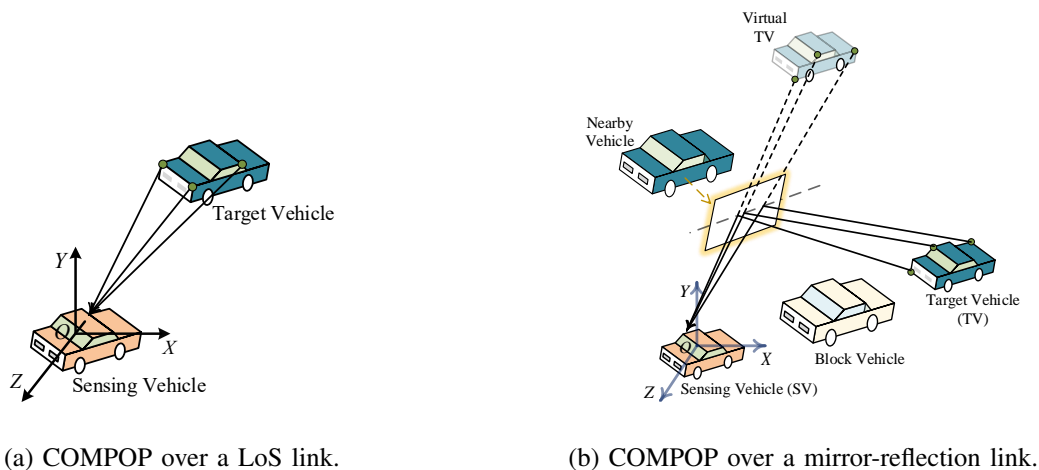


Figure 1: Two scenarios of COMPOP.

II. SYSTEM MODEL

Consider the scenario with multiple vehicles on the road, including one pair of TV and SV. The TV is equipped with an antenna array with N_t elements distributed over the vehicle body such that the distribution sketches its shape. Consequently, the SV equipped with a distributed array of N_r antennas performs multi-point positioning of the TV by locating its antennas from their broadcast waveforms in a mmWave spectrum. As illustrated in Fig. 1, we consider both the scenarios where the TV and SV are connected with an LoS link or NLoS links. For the scenario of NLoS links [see Fig. 1(b)], COMPOP at the SV relies on signals reflected on the smooth surfaces of nearby vehicles. Though mmWave signals are attenuated severely by scattering and reflection on non-smooth surfaces, the attenuation is found to be small if the surfaces are smooth, e.g., those of vehicles' polished metallic body [19].

A. Signal Models

Each TV antenna transmits the superposition of two waveforms for facilitating different operations of COMPOP. One is a signature waveform (a multi-tone waveform) transmission (similar to that in [20]) enabling the SV to estimate the SV-TV system clock difference so as to eliminate its negative effect on the positioning. The second is a SFCW waveform (also a multi-tone waveform) in a separate bandwidth from the signature, which facilitates COMPOP at the SV. The waveforms are described as follows.

1) *Signature Waveform*: For clock-difference estimation, it is sufficient to transmit different signature waveforms over two antennas, whose indices are denoted as a and b , using two single

tones for each antenna. The antenna coordinates are represented as $\mathbf{x}_a = (x_a, y_a, z_a)$ and $\mathbf{x}_b = (x_b, y_b, z_b)$, respectively. The two waveforms for the two antennas, denoted as s_a and s_b , are given as

$$s_a(t + \sigma) = e^{j2\pi f_a(t+\sigma)} + e^{j2\pi(f_a+\Delta)(t+\sigma)}, \quad s_b(t + \sigma) = e^{j2\pi f_b(t+\sigma)} + e^{j2\pi(f_b+\Delta)(t+\sigma)}, \quad (1)$$

where f_a and f_b are two orthogonal frequencies specifying the signatures, Δ is a given frequency separation, and σ is the TV-SV system clock difference (in sec).

First, consider the scenario with L surface-reflection links ($L \geq 1$). Let $\Gamma^{(\ell)}$ denote the complex reflection coefficient of the ℓ -th link given as $\Gamma^{(\ell)} = |\Gamma^{(\ell)}| \exp(j\angle\Gamma^{(\ell)})$. Moreover, let $\tau_{n,m}^{(\ell)}$ denote the signal flight time from TV's antenna n to SV's antenna m proportional to the propagation distance $d_{n,m}^{(\ell)}$, i.e., $d_{n,m}^{(\ell)} = c \cdot \tau_{n,m}^{(\ell)}$ where c is the speed of light. Given the notations above, the raw received waveform at each SV antenna, say antenna m , is given as

$$W_m = \sum_{\ell=1}^L w_m^{(\ell)}(t), \quad (2)$$

where $w_m^{(\ell)}(t) = \Gamma^{(\ell)} s_a(t + \sigma - \tau_{a,m}^{(\ell)}) + \Gamma^{(\ell)} s_b(t + \sigma - \tau_{b,m}^{(\ell)})$. We assume that the AoAs of different signal arrivals are separable using a classic technique, e.g., MUSIC [21], where the AoAs can be accurately detected in the angular domain by searching the power spectrum of the received signals¹. Specifically, after AoA detection, the received signals can be differentiated by coherent detection in the angular domain, and regrouped as a vector $\mathbf{w}_m = [w_m^{(1)}(t), \dots, w_m^{(L)}(t)]^T$. Note that each element in \mathbf{w}_m comprises waveforms at four different frequencies. By exploiting frequency orthogonality, different frequency components in the received waveform antenna m , can be separated and grouped to form two K by L matrices to facilitate the algorithmic design in the sequel:

$$\mathbf{A}_m(t) = [\mathbf{a}_m^{(1)}(t), \dots, \mathbf{a}_m^{(L)}(t)], \quad \mathbf{B}_m(t) = [\mathbf{b}_m^{(1)}(t), \dots, \mathbf{b}_m^{(L)}(t)], \quad (3)$$

where

$$\mathbf{a}_m^{(\ell)}(t) = \Gamma^{(\ell)} \begin{bmatrix} e^{j2\pi f_a(t+\sigma-\tau_{a,m}^{(\ell)})} \\ e^{j2\pi(f_a+\Delta)(t+\sigma-\tau_{a,m}^{(\ell)})} \end{bmatrix}, \quad \mathbf{b}_m^{(\ell)}(t) = \Gamma^{(\ell)} \begin{bmatrix} e^{j2\pi f_b(t+\sigma-\tau_{b,m}^{(\ell)})} \\ e^{j2\pi(f_b+\Delta)(t+\sigma-\tau_{b,m}^{(\ell)})} \end{bmatrix}. \quad (4)$$

¹The effect of antennas on AoA detection accuracy is well studied by simulations in [22] such that AoA error is significantly reduced as the number of antenna increases.

Next, two matched filters are designed as $\mathbf{D}_a = \text{diag} \{e^{-j2\pi f_a t}, e^{-j2\pi(f_a+\Delta)t}\}$ and $\mathbf{D}_b = \text{diag} \{e^{-j2\pi f_b t}, e^{-j2\pi(f_b+\Delta)t}\}$, for demodulating $\mathbf{A}_m(t)$ and $\mathbf{B}_m(t)$ from time functions into matrix symbols:

$$\mathbf{A}_m = \mathbf{D}_a \mathbf{A}_m(t) = [\mathbf{a}_m^{(1)}, \mathbf{a}_m^{(2)}, \dots, \mathbf{a}_m^{(L)}] \quad (5)$$

$$\mathbf{B}_m = \mathbf{D}_b \mathbf{B}_m(t) = [\mathbf{b}_m^{(1)}, \mathbf{b}_m^{(2)}, \dots, \mathbf{b}_m^{(L)}], \quad (6)$$

where

$$\mathbf{a}_m^{(\ell)} = \Gamma^{(\ell)} \begin{bmatrix} e^{j2\pi f_a(\sigma - \tau_{a,m}^{(\ell)})} \\ e^{j2\pi(f_a+\Delta)(\sigma - \tau_{a,m}^{(\ell)})} \end{bmatrix}, \quad \mathbf{b}_m^{(\ell)} = \Gamma^{(\ell)} \begin{bmatrix} e^{j2\pi f_b(\sigma - \tau_{b,m}^{(\ell)})} \\ e^{j2\pi(f_b+\Delta)(\sigma - \tau_{b,m}^{(\ell)})} \end{bmatrix}. \quad (7)$$

It is worthwhile to notice that all equations above also hold if one of the L links is a LoS link.

Next, consider the other scenario with a LoS link to the TV, where unresolvable reflection links possibly exist but are neglected due to the significant power difference between LoS and NLoS paths. Without loss of generality, let the resultant uniform channel gains be normalized as $\Gamma = 1$. Then the LoS counterparts of \mathbf{A}_m and \mathbf{B}_m can be simplified from (5) and (6) as:

$$\mathbf{A}_m^{\text{LOS}} = \begin{bmatrix} e^{j2\pi f_a(\sigma - \tau_{a,m})} \\ e^{j2\pi(f_a+\Delta)(\sigma - \tau_{a,m})} \end{bmatrix}, \quad \mathbf{B}_m^{\text{LOS}} = \begin{bmatrix} e^{j2\pi f_b(\sigma - \tau_{b,m})} \\ e^{j2\pi(f_b+\Delta)(\sigma - \tau_{b,m})} \end{bmatrix}. \quad (8)$$

where $\tau_{n,m}$ denotes the signal flight time from TV's antenna n to SV's antenna m proportional to the propagation distance $d_{n,m}$ in LoS.

2) *SFCW Waveform*: A multi-tone waveform commonly used in RADAR, called *stepped-frequency-continuous-wave* (SFCW) [12], [13], [23], is broadcast by each TV antenna. The waveform, denoted as $s(t)$, comprises multiple single-tone continuous-waves with equally separated frequencies by a fixed frequency gap Δ . Mathematically,

$$s(t) = \sum_{k=1}^K \exp(j2\pi f_k t), \quad (9)$$

where $\mathcal{F} = \{f_k\}_{k=1}^K$ represents the set of frequencies such that $f_k = f_1 + (k-1)\Delta$ for $k = 1, \dots, K$. The vector form of the SFCW is also provided as

$$\mathbf{s}(t) = [\exp(j2\pi f_1 t), \dots, \exp(j2\pi f_K t)]^T, \quad (10)$$

since the single-tone continuous-waves are naturally separated in frequency.

First, consider the scenario with L surface-reflection links ($L \geq 1$). With frequency decoupling, the received signal at the SV's antenna m is

$$\mathbf{r}_m(t) = \sum_{\ell=1}^L \mathbf{r}_m^{(\ell)}(t), \quad (11)$$

where $\mathbf{r}_m^{(\ell)}(t) \in \mathbb{C}^{K \times 1}$ represents the signal vector from the ℓ -th surface-reflection link as

$$\mathbf{r}_m^{(\ell)}(t) = \Gamma^{(\ell)} \sum_{n=1}^{N_t} \mathbf{r}_{n,m}^{(\ell)}(t) = \Gamma^{(\ell)} \sum_{n=1}^{N_t} \mathbf{s}(t + \sigma - \tau_{n,m}^{(\ell)}). \quad (12)$$

By assuming perfect AoA detection using the MUSIC technique [21], we can decompose (11) into individual $\mathbf{r}_m^{(\ell)}(t)$ by coherent detection in the angular domain, which is rewritten as a K by L matrix $\mathbf{R}_m(t)$ as follows:

$$\mathbf{R}_m(t) = [\mathbf{r}_m^{(1)}(t), \dots, \mathbf{r}_m^{(L)}(t)]. \quad (13)$$

Assuming that the TV-SV system clock difference σ is estimated as $\tilde{\sigma}$, the received signal (13) is demodulated by multiplying the K by K matched filtering matrix $\mathbf{D} = \text{diag}\{\mathbf{s}(t + \tilde{\sigma})^H\}$ as

$$\mathbf{Y}_m = [\mathbf{y}_m^{(1)}, \dots, \mathbf{y}_m^{(L)}] = \mathbf{D}\mathbf{R}_m(t), \quad (14)$$

where $\mathbf{y}_m^{(\ell)} = \mathbf{D}\mathbf{r}_m^{(\ell)}(t) = [y_m^{\ell,1}, y_m^{\ell,2}, \dots, y_m^{\ell,K}]^T$ with the component $y_m^{\ell,k}$ being

$$y_m^{\ell,k} = \Gamma^{(\ell)} \sum_{n=1}^{N_t} \exp[j2\pi f_k(\sigma - \tilde{\sigma} - \tau_{n,m}^{(\ell)})]. \quad (15)$$

With accurate estimation of the clock difference using the algorithm in Section III-A, the (ℓ, k) -th received signal component is simplified as

$$y_m^{\ell,k} = \Gamma^{(\ell)} \sum_{n=1}^{N_t} \exp[-j2\pi f_k \tau_{n,m}^{(\ell)}], \quad \forall \ell, k. \quad (16)$$

Next, consider the other scenario with a LoS link. The received signal component in (16) can be further simplified with $\Gamma = 1$ as

$$y_m^k = \sum_{n=1}^{N_t} \exp[-j2\pi f_k \tau_{n,m}], \quad \forall k. \quad (17)$$

Moreover, without loss of generality, we define the origin O of the coordinate system at the center of the SV, Z -axis in the direction of AoA. The X , Y -axes are parallel and vertical to the ground, respectively, perpendicular to the Z -axis, as shown in Fig. 1.

Remark 1 (Feasible Ranging Distance of SFCW). Due to the periodicity of phases, the maximum ranging distance of SFCW should be limited by $R_{\max} = \frac{c}{\Delta}$ (in meters) to avoid ambiguity [13].

Remark 2 (Channel Fading). The sampling process takes $T_s = \frac{1}{\mathcal{B}}$ seconds, where \mathcal{B} is the system bandwidth at the SV. Since the sampling duration (3.3^{-10} s with $\mathcal{B} = 3$ GHz) is much shorter than the coherence time (approximately $T_c = 1$ ms at 30 GHz with velocity $v = 10$ m/s [24]), the channel fading, comprising the pathloss and small-scale fading, is considered as a constant and omitted in the presentation for convenience.

B. Procedure Design

For their non-overlapping spectrums, the two waveforms can be separated by the SV using filtering. Moreover, the signal processing delay at the SV is fixed and known from calibration, allowing the suppression of its effect on TV positioning.

1) *Clock Synchronization*: To establish direct relation between the TV's multi-point position and the superimposed signal $y_m^{\ell,k}$ (16) or y_m^k (17), the SV aims at compensating the system clock difference σ by using (5), (6) or (8), divided into two cases as follows.

- **A LoS link**: When a LoS link exists, the SV is expected to detect the system clock difference σ from the received signature waveforms $\{\mathbf{A}_m^{\text{LOS}}, \mathbf{B}_m^{\text{LOS}} \mid \forall m\}$, where $\mathbf{A}_m^{\text{LOS}}, \mathbf{B}_m^{\text{LOS}}$ are matrix signals in (8) received over the m -th antenna.
- **Reflection links**: The clock synchronization needs to be achieved for each reflection link. Take the ℓ -th reflection link as an example, the clock difference σ needs to be detected based on signature waveforms $\{\mathbf{a}_m^{(\ell)}, \mathbf{b}_m^{(\ell)} \mid \forall m\}$, where $\mathbf{a}_m^{(\ell)}, \mathbf{b}_m^{(\ell)}$ are given in (7).

2) *Multi-point Positioning*: Define the set of transmit-antenna locations at a TV as $\mathcal{X} = \{\mathbf{x}_n\}$ with $\mathbf{x}_n \in \mathbb{R}^3$ and $|\mathcal{X}| = N_t$. Then, an indicator function $\mathbb{I}_{\{\mathbf{x} \in \mathcal{X}\}}$ to represent the transmit antenna's distribution over the 3D spatial domain is defined as

$$\mathbb{I}_{\{\mathbf{x} \in \mathcal{X}\}} = \sum_{n=1}^{N_t} \delta(\mathbf{x} - \mathbf{x}_n), \quad (18)$$

where $\delta(\cdot)$ is a delta function satisfying $\delta(\mathbf{x}) = 0, \forall \mathbf{x} \neq \mathbf{0}$ and $\int_{\mathbb{R}^3} \delta(\mathbf{x}) d\mathbf{x} = 1$. Let $D(\mathbf{x}_n, \mathbf{p}_m) = \|\mathbf{x}_n - \mathbf{p}_m\|$ measures the LoS distance between \mathbf{x}_n and the location of receive antenna m denoted by \mathbf{p}_m . For reflection links, $D^{(\ell)}(\mathbf{x}_n, \mathbf{p}_m)$ measures the propagation distance over the ℓ -th link. Accordingly, we directly have $\tau_{n,m} = \frac{D(\mathbf{x}_n, \mathbf{p}_m)}{c}$ and $\tau_{n,m}^{(\ell)} = \frac{D^{(\ell)}(\mathbf{x}_n, \mathbf{p}_m)}{c}$. Also, the received SFCW waveforms (16) and (17) can be rewritten as

$$y_m^{\ell,k} = \Gamma^{(\ell)} \sum_{n=1}^{N_t} \exp\left(-j \frac{2\pi f_k}{c} D^{(\ell)}(\mathbf{x}_n, \mathbf{p}_m)\right), \quad \forall \ell, k. \quad (19)$$

for reflection links and

$$y_m^k = \sum_{n=1}^{N_t} \exp\left(-j \frac{2\pi f_k}{c} D(\mathbf{x}_n, \mathbf{p}_m)\right), \quad \forall k. \quad (20)$$

for the LoS link if it exists.

As aforementioned, the point set \mathcal{X} represents the multi-point position information of the TV. Estimating \mathcal{X} can be divided into two cases as follows.

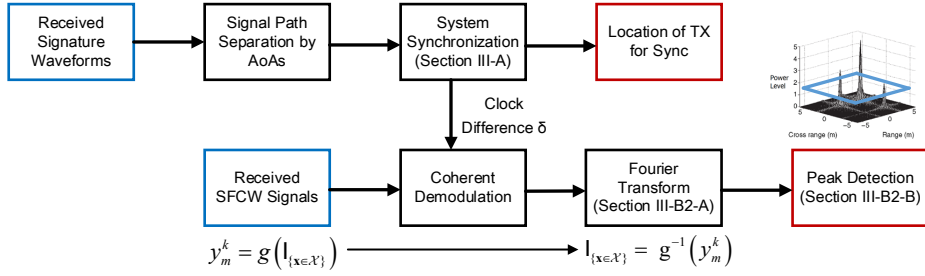


Figure 2: Diagram of COMPOP in LoS.

- **A LoS link:** The multi-point TV position \mathcal{X} is directly retrieved from SFCW signals received in LoS, i.e., $\{y_m^k \mid \forall m, k\}$.
- **Reflection Links:** The real multi-point TV position \mathcal{X} needs to be detected by combining all SFCW signals from different reflection links, i.e., $\{y_m^{(\ell)} \mid \forall m, \ell\}$.

III. COMPOP OVER A LOS LINK

In this section, we consider a case where a LoS link between the TV and the SV exists, making it reasonable to ignore other reflection links due to the significant power difference between LoS and NLoS paths. The scheme we propose for LoS case is illustrated in Fig. 2, consisting of two steps: 1) synchronization; and 2) multi-point positioning. The overview and algorithm description for each step are presented in the following.

For clarification, we firstly summarized the assumptions used in this section:

- **Perfect AoA Detection:** Accurate AoA detection can be realized by applying classical MUSIC algorithm [21] with an appropriate number of antennas at the receiver.
- **Constant Channel Fading:** The channel fading is considered constant during the sampling process.

A. Step 1: Synchronization

1) *Overview:* As illustrated in Sec. II-A, synchronization is necessary to compensate the system clock difference σ , enabling correct coherent demodulation (14) at the receiver and the subsequent multi-point positioning. Note that the clock difference is contained in the signal phases in (8), which can be observed at the receiver. However, to estimate the clock difference σ directly is challenging because it is coupled with the propagation delay τ_m as shown in (8). Therefore, it is necessary to separate the two parameters by estimating the propagation delay first, which can be translated into the estimation of one representative transmit antenna, say \mathbf{x}_a ,

given the knowledge of the receive antennas' locations. To this end, we first estimate \mathbf{x}_a in the presence of noise by applying a *phase-difference-of-arrival* (PDoA) based method [9], [25].

2) *Algorithm Description*: Here we give an approach to estimate the location \mathbf{x}_a of the representative transmit antenna a from the received signature waveform $\mathbf{A}_m^{\text{LOS}}$ in (8). The index of the transmit antenna are omitted for brevity, i.e. $\tau_m = \tau_{a,m}$.

- *Detection of TX Location*: Let $F_m(\mathbf{x}_a)$ denote the propagation distance difference from the antenna a to the SV's antennas m and 1, given as

$$F_m(\mathbf{x}_a) = D(\mathbf{x}_a, \mathbf{p}_m) - D(\mathbf{x}_a, \mathbf{p}_1), \quad m = 2, \dots, N_r. \quad (21)$$

At the SV's antenna m , the phase difference $\eta_m = 2\pi\Delta(\tau_m - \sigma)$ between the two components of the received signature waveforms can be directly measured from $\mathbf{A}_m^{\text{LOS}}$ in (8) with noise in the presence, denoted as $\tilde{\eta}_m$. Then based on the relation $\eta_m = 2\pi\Delta(\tau_m - \sigma) = 2\pi\Delta\left(\frac{D(\mathbf{x}_a, \mathbf{p}_m)}{c} - \sigma\right)$, a noisy measurement of $F_m(\mathbf{x}_a)$ is given as

$$\tilde{F}_m = c \frac{(\tilde{\eta}_m - \tilde{\eta}_1)}{2\pi\Delta} = c \frac{(\eta_m - \eta_1)}{2\pi\Delta} + \Delta\varphi_m, \quad m = 2, \dots, N_r, \quad (22)$$

where $\Delta\varphi_m$ is the additional Gaussian noise. Since $F_m(\mathbf{x}_a)$ is univariate w.r.t. the location \mathbf{x}_a , the TX location can be optimized based on the *minimum-mean-square-error* (MMSE) criterion to minimize the gap between $F_m(\mathbf{x}_a)$ and the measurement \tilde{F}_m as follows.

Problem 1 (TX Location Optimization).

$$\min_{\mathbf{x}_a} \sum_{m=1}^{N_r} \left\| \tilde{F}_m - F_m(\mathbf{x}_a) \right\|_2^2. \quad (23)$$

Then the optimal solution \mathbf{x}_a^* , which naturally coincides with the actual location \mathbf{x}_a , can be achieved by using the iterative Gauss-Newton method [26] with an arbitrary initial point $\tilde{\mathbf{x}}_a$ as follows

$$\mathbf{h} = (\mathbf{G}(\tilde{\mathbf{x}}_a)^T \mathbf{G}(\tilde{\mathbf{x}}_a))^{-1} \mathbf{G}(\tilde{\mathbf{x}}_a)^T \mathbf{b}(\tilde{\mathbf{x}}_a) \quad (24)$$

$$\tilde{\mathbf{x}}_a \leftarrow \tilde{\mathbf{x}}_a + \mathbf{h},$$

where

$$\mathbf{G}(\tilde{\mathbf{x}}_a) = \begin{bmatrix} \frac{\partial F_2(\tilde{\mathbf{x}}_a)}{\partial x_a} & \frac{\partial F_2(\tilde{\mathbf{x}}_a)}{\partial y_a} & \frac{\partial F_2(\tilde{\mathbf{x}}_a)}{\partial z_a} \\ \dots & \dots & \dots \\ \frac{\partial F_{N_r}(\tilde{\mathbf{x}}_a)}{\partial x_a} & \frac{\partial F_{N_r}(\tilde{\mathbf{x}}_a)}{\partial y_a} & \frac{\partial F_{N_r}(\tilde{\mathbf{x}}_a)}{\partial z_a} \end{bmatrix}, \quad \mathbf{b}(\tilde{\mathbf{x}}_a) = \begin{bmatrix} \tilde{F}_2 - F_2(\tilde{\mathbf{x}}_a) \\ \dots \\ \tilde{F}_{N_r} - F_{N_r}(\tilde{\mathbf{x}}_a) \end{bmatrix}. \quad (25)$$

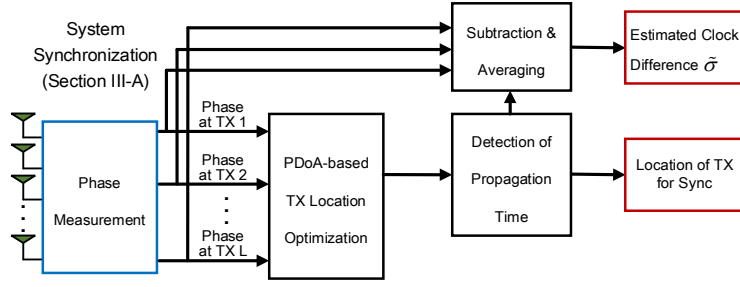


Figure 3: Diagram of the system clock synchronization process.

- *Detection of Propagation Time:* With the knowledge of \mathbf{x}_a , the propagation time τ_m can be detected for signals at receive antenna m by $\tau_m = \frac{D(\mathbf{x}_a, \mathbf{p}_m)}{c}$.
- *Subtraction & Averaging:* By subtracting the propagation time τ_m component from the noisy phase measurement $\tilde{\eta}_m$, the system clock difference can be differently calculated depending on the choice of the SV's antenna m , denoted by $\tilde{\sigma}_m = \tau_m - \frac{\tilde{\eta}_m}{2\pi\Delta}$. Averaging these values gives an accurate estimate of σ such that $\tilde{\sigma} = \sum_{m=1}^{N_r} \tilde{\sigma}_m$.

Proposition 1 (Synchronization Feasibility Condition). At least four SV's antennas are required ($N_r \geq 4$) to detect the TV-SV system clock difference, according to the solution of (23) in [26].

Note that although such an approach is based on a similar principle to the method in [9], we give a new design to output a clock difference estimation. Moreover, one more antenna location \mathbf{x}_b can be detected by applying the same algorithm above on the signature waveform $\mathbf{B}_m^{\text{LOS}}$ in (8) at the receiver. The detected locations \mathbf{x}_a , \mathbf{x}_b of the representative transmit antennas help the COMPOP over the reflection links illustrated later in Section IV-B.

Remark 3 (TV Recognition in LoS). In LoS case, the SV is able to resolve signals from different TVs according to the AoAs with an antenna array [21]. Considering the signature waveform and SFCW transmissions share the same signal paths, the clock difference detected from signature waveforms will be used for SFCWs with the same AoAs, and the multi-point TV position detected in Sec. III-B will be mapped to the same AoAs as well.

Remark 4 (Initial Value Selection). It is recommended to use a solution satisfying any three equations in

$$\tilde{F}_m = D(\mathbf{x}_a, \mathbf{p}_m) - D(\mathbf{x}_a, \mathbf{p}_1), \quad m = 2, \dots, N_r. \quad (26)$$

as the initial selection of $\tilde{\mathbf{x}}_a$, where the convergence to the global optimal is verified by simulations.

Remark 5 (Sampling Requirement). The synchronization procedures are based on the assumption that the phase gap estimated at each two adjacent receive antennas is no larger than $\frac{\pi}{2}$. Thus the distance between each two adjacent receive antenna at the SV needs to satisfy $\Delta_d < \frac{c}{2\Delta}$.

Proposition 2 (Error Covariance). We use the error covariance matrix $\text{cov}(\tilde{\mathbf{x}}_a)$ as the performance metric of the above synchronization approach, defined as

$$\text{cov}(\tilde{\mathbf{x}}_a) = \mathbb{E} \left[(\tilde{\mathbf{x}}_a - \mathbb{E}[\tilde{\mathbf{x}}_a]) (\tilde{\mathbf{x}}_a - \mathbb{E}[\tilde{\mathbf{x}}_a])^T \right]. \quad (27)$$

For tractability, we assume that the phase error follows an *independent identically distributed* (i.i.d.) Gaussian distribution where $\Delta\varphi_m \sim \mathcal{N}(0, \sigma_z^2 \mathbf{I})$, $\forall m$. As the number of SV's antennas N_r becomes larger, the covariance matrix $\text{cov}(\tilde{\mathbf{x}}_a)$ scales with $\mathcal{O}\left(\frac{1}{N_r-1}\right)$.

Proof: See Appendix A. □

According to Proposition 2, we assume perfect synchronization in the following steps for convenience. However, in simulations, we keep the phase noise and the resultant clock difference detection error through the entire process.

Remark 6 (Comparison with Existing Synchronization Methods). Such a clock synchronization method clearly differs from conventional GPS-based approaches [27] since it does not rely on the GPS. Compared to consensus-based synchronization approaches [28], the method we proposed can be processed in real time and thus is more suitable for vehicular sensing.

B. Step 2: Multi-Point Positioning

1) *Overview:* As shown in Fig. 2, the system clock difference σ can be removed by the preceding step, facilitating the following procedures. The main idea of the multi-point positioning step in LoS is briefly illustrated as follows. We first show that the received signal y_m^k can be presented as a function of the indicator $l_{\{\mathbf{x} \in \mathcal{X}\}}$ which represents the power spectrum of the transmit antennas, denoted as $y_m^k = g(l_{\{\mathbf{x} \in \mathcal{X}\}})$. Therefore, the position information \mathcal{X} of the TV can be retrieved from the received signals through an inverse function and a following peak detection. We give the estimation of \mathcal{X} in the following algorithm, divided into two phases 1) Fourier transform; and 2) peak detection, as described in Fig. 2.

2) *Algorithm Description:* The synchronized demodulation (17) enables to express y_m^k as (20), which can be rewritten in a 3D surface integral form as

$$y_m^k = y(\mathbf{p}_m, f_k) = \int_{\mathbb{R}^3} l_{\{\mathbf{x} \in \mathcal{X}\}} \exp\left(-j \frac{2\pi f_k}{c} D(\mathbf{x}, \mathbf{p}_m)\right) d\mathbf{x}, \quad (28)$$

Table I: Fourier Transform Pairs

Fourier Transform	Inverse Fourier Transform
$\text{FT}_{2\text{D}}(\mathbf{h}(\mathbf{x})) = \int_{\mathbb{R}^2} \mathbf{h}(\mathbf{x}) \exp(-j\frac{2\pi}{c} \mathbf{f}^T \mathbf{x}) dx dy$	$\text{FT}_{2\text{D}}^{-1}(\mathbf{H}(\mathbf{f})) = \int_{\mathbb{R}^2} \mathbf{H}(\mathbf{f}) \exp(j\frac{2\pi}{c} \mathbf{f}^T \mathbf{x}) df^{(x)} df^{(y)}$
$\text{FT}_{3\text{D}}(\mathbf{h}(\mathbf{x})) = \int_{\mathbb{R}^3} \mathbf{h}(\mathbf{x}) \exp(-j\frac{2\pi}{c} \mathbf{f}^T \mathbf{x}) d\mathbf{x}$	$\text{FT}_{3\text{D}}^{-1}(\mathbf{H}(\mathbf{f})) = \int_{\mathbb{R}^3} \mathbf{H}(\mathbf{f}) \exp(j\frac{2\pi}{c} \mathbf{f}^T \mathbf{x}) d\mathbf{f}$
$\text{FT}_{2\text{D}}^D(\{\mathbf{h}[x, y]\})$ $= \sum_{n_x=-\infty}^{\infty} \sum_{n_y=-\infty}^{\infty} \mathbf{h}[x, y] \exp(-j\frac{2\pi}{c} (f^{(x)} n_x + f^{(y)} n_y))$	$\text{FT}_{2\text{D}}^{D^{-1}}(\mathbf{H}(\mathbf{f}))$ $= \int_{\mathbb{R}^2} \mathbf{H}(\mathbf{f}) \exp(j\frac{2\pi}{c} (f^{(x)} n_x + f^{(y)} n_y)) df^{(x)} df^{(y)}$
$\text{FT}_{3\text{D}}^D(\{\mathbf{h}[x, y, z]\})$ $= \sum_{n_x=-\infty}^{\infty} \sum_{n_y=-\infty}^{\infty} \sum_{n_z=-\infty}^{\infty} \mathbf{h}[x, y, z] \exp(-j\frac{2\pi}{c} \mathbf{f}^T \mathbf{n}_{\mathbf{x}})$	$\text{FT}_{3\text{D}}^{D^{-1}}(\mathbf{H}(\mathbf{f})) = \int_{\mathbb{R}^3} \mathbf{H}(\mathbf{f}) \exp(j\frac{2\pi}{c} \mathbf{f}^T \mathbf{n}_{\mathbf{x}}) d\mathbf{f}$
$\mathbf{x} = (x, y, z)^T$ represents a vector in 3D space, and $\mathbf{f} = (f^{(x)}, f^{(y)}, f^{(z)})^T$ represents a vector in 3D frequency domain, and $\mathbf{n}_{\mathbf{x}} = (n_x, n_y, n_z)^T$ denotes the index of the sample $\mathbf{h}[x, y, z]$ in the set $\{\mathbf{h}[x, y, z]\}$.	

where $y(\mathbf{x}, f) : \mathbb{R}^4 \rightarrow \mathbb{R}$ is a continuous function, and $D(\mathbf{x}, \mathbf{p}_m) = \|\mathbf{x} - \mathbf{p}_m\|$ represents the Euclidean distance between point $\mathbf{x} = (x, y, z)^T$ and the location of the SV's antenna m , denoted by $\mathbf{p}_m = (p_m^{(x)}, p_m^{(y)}, p_m^{(z)})^T$. Then based on (28), we have the following lemma based on the scalar diffraction idea in [29].

Lemma 1. Consider the indicator function of transmit antennas $\mathbb{1}_{\{\mathbf{x} \in \mathcal{X}\}}$ and the function $y(\mathbf{x}, f)$ representing signals at the receiver. The following equality holds in the frequency domain as

$$\text{FT}_{2\text{D}}(s(x, y, f)) \Big|_{f=\|\mathbf{f}\|} = \text{FT}_{3\text{D}}(\mathbb{1}_{\{\mathbf{x} \in \mathcal{X}\}}). \quad (29)$$

where $\mathbf{f} = (f^{(x)}, f^{(y)}, f^{(z)})^T$ is a spatial frequency vector, and $s(x, y, f) = y(x, y, 0, f)$ is a continuous function, representing received signals at the $X - Y$ plane $z = 0$. The $\text{FT}_{2\text{D}}(\cdot)$ and $\text{FT}_{3\text{D}}(\cdot)$ are 2D and 3D Fourier transforms defined in Table I.

Proof: Please refer to Appendix B. □

Remark 7 (Sampling at the Receiver). Based on the received signals, we are only able to collect samples of $y(\mathbf{x}, f)$ discretely over the receive antenna array. Recall that Z -axis is in the direction of AoA known at the SV, leading to the following approximation

$$s(p_m^{(x)}, p_m^{(y)}, f_k) = y(p_m^{(x)}, p_m^{(y)}, 0, f_k) \approx y(\mathbf{p}_m, f_k) \exp\left(-j\frac{2\pi f_k}{c} p_m^{(z)}\right), \quad (30)$$

which holds tightly when the TV-SV distance is much larger than the SV's size. Therefore, based on the approximation in (30), discrete samples on $s(x, y, f)$ are also available.

Remark 8 (Linear Interpolation). Since the receive antennas may not be regularly distributed, a linear interpolation [30] is adopted to provide samples of $s(x, y, f)$ uniformly spaced along the X and Y directions. Take samples at two adjacent receive antennas in the X direction as an example, whose coordinates are supposed to be \mathbf{p}_{m_1} and \mathbf{p}_{m_2} , and $p_{m_1}^{(y)} = p_{m_2}^{(y)}$. Then the interpolation generates samples between these two points as

$$s(x, p_{m_1}^{(y)}, f) = \frac{x - p_{m_1}^{(x)}}{p_{m_2}^{(x)} - p_{m_1}^{(x)}} s(p_{m_2}^{(x)}, p_{m_2}^{(y)}, f) + \frac{p_{m_2}^{(x)} - x}{p_{m_2}^{(x)} - p_{m_1}^{(x)}} s(p_{m_1}^{(x)}, p_{m_1}^{(y)}, f), \quad p_{m_1}^{(x)} < x < p_{m_2}^{(x)}. \quad (31)$$

By using interpolation in (31) along X and Y directions sequentially, continuous samples of $s(x, y, f)$ are generated on the plane $z = 0$, and uniformly spaced samples are available as well. The samples of $s(x, y, f)$ after the interpolation are denoted as $\{s[x, y, f]\}$. Since SFCW signals are used, the samples are naturally discrete and uniformly spaced in frequency.

It is also worthwhile to notice that common interpolation methods, e.g., linear, spline and polynomial interpolations are all capable of accurate resampling here. Therefore, we simply adopt linear interpolation for low-complexity and the interpolation error is omitted in the following presentation for convenience.

Moreover, to preserve complete information in the frequency domain with discrete samples, the distances between two adjacent receive antennas along X or Y directions are both required to be less than $\frac{c}{2(f_1 + f_K)}$ according to the Nyquist sampling criterion, which will be elaborated later in Sec. III-C. Here we simply assume that the samplings at the receiver satisfy the Nyquist criterion and the interpolation is accurate. Then the LHS of (29) with discrete inputs turns to be

$$\text{FT}_{2\text{D}}^D (\{s[x, y, f]\}) = S(f^{(x)}, f^{(y)}, f), \quad (32)$$

where $\text{FT}_{2\text{D}}^D$ refers to the 2D discrete-time Fourier transform defined in Table I, and the output $S(f^{(x)}, f^{(y)}, f)$ is a function continuous in $f^{(x)}$ and $f^{(y)}$ domain while discrete in f direction. By considering $S(f^{(x)}, f^{(y)}, f)$ as a function of \mathbf{f} according to the relation $f = \|\mathbf{f}\|$, the continuous function $\{S(\mathbf{f}) | \forall \mathbf{f} \in \mathbb{R}^3\}$ over the 3D frequency domain can be estimated by an interpolation [30]. Then the LHS of (29) can be approximated as

$$\text{FT}_{2\text{D}} (s(x, y, f)) |_{f=\|\mathbf{f}\|} \approx \text{L} \left(S(f^{(x)}, f^{(y)}, f) |_{f=\|\mathbf{f}\|} \right) = \text{L} \left(\text{FT}_{2\text{D}}^D (\{s[x, y, f]\}) |_{f=\|\mathbf{f}\|} \right), \quad (33)$$

where $\text{L}(\cdot)$ represents the linear interpolation process [30].

On the other hand, the RHS of (29) can be represented in the discrete case as $\text{FT}_{3\text{D}}^D (\{ \{ I_{\{\mathbf{x} \in \mathcal{X}\}} \} \})$, where $\text{FT}_{3\text{D}}^D$ is the 3D discrete-time Fourier transform. Then according to (33), the equality in (29) directly gives

$$\mathcal{L} \left(\text{FT}_{2\text{D}}^D (\{ \mathfrak{s}[x, y, f] \}) \Big|_{f=\|\mathbf{f}\|} \right) \approx \text{FT}_{3\text{D}}^D (\{ \{ I_{\{\mathbf{x} \in \mathcal{X}\}} \} \}). \quad (34)$$

The approximation in (34) comes from the interpolation process, which is proved to be accurate by simulations.

- *A. Fourier Transform:* According to (34), the indicator function $I_{\{\mathbf{x} \in \mathcal{X}\}}$ can be estimated in a discrete form via a 3D inverse discrete-time Fourier transform as

$$\Phi[\mathbf{x}] = \text{FT}_{3\text{D}}^{D^{-1}} \left\{ \mathcal{L} \left(\text{FT}_{2\text{D}}^D (\{ \mathfrak{s}[x, y, f] \}) \Big|_{f=\|\mathbf{f}\|} \right) \right\} \approx \{ \{ I_{\{\mathbf{x} \in \mathcal{X}\}} \} \}. \quad (35)$$

- *B. Peak Detection:* Locations of the transmit antennas can be estimated by peak detection over the power spectrum $\{ |\Phi[\mathbf{x}]| \}$ after a power normalization, namely,

$$\mathcal{X} = \left\{ \mathbf{x} \mid \frac{|\Phi[\mathbf{x}]|}{\{ |\Phi[\mathbf{x}]| \}_{\max}} \geq \nu \right\}, \quad (36)$$

where ν represents the detection threshold appropriately selected, and $\{ |\Phi[\mathbf{x}]| \}_{\max}$ is the maximum value of the detected power spectrum $\{ |\Phi[\mathbf{x}]| \}$.

Therefore, according to the algorithm above, the multi-point TV position can be retrieved from signals over the antenna array at the receiver, for the LoS case.

C. Resolution Analysis

This subsection provides analysis on resolution of the multi-point position retrieved by the above algorithm. Here we consider the 3D antenna array at the receiver as an ‘equivalent aperture’ located in the $X - Y$ plane $z = 0$, as shown in Fig. 4(a).

For ease of understanding, we first introduce the following terminologies.

Definition 1 (Bandwidth). A bandwidth \mathcal{B} in a direction of the frequency domain (at the receiver) is defined as the maximum frequency difference of the received signal along the corresponding direction in the spatial domain.

Definition 2 (Resolution). A resolution δ , representing the positioning accuracy, is defined as the minimum distance to differentiate multiple objects, TV’s antennas in our work. The resolution is said to be better when the minimum distance is smaller. Accordingly, resolutions in X or Y directions and Z direction are respectively called the *azimuth* and *range* resolutions.

The direct relation between bandwidth \mathcal{B} and resolution δ is established as

$$\delta = \frac{c}{\mathcal{B}}, \quad (37)$$

where c is the light speed. Based on this relation, the azimuth and range resolutions are firstly analyzed, and then sampling requirements to achieve a given resolution are provided next.

1) *Azimuth Resolution:* Suppose the detected TV position \mathcal{X} of (36) is projected on the equivalent aperture's center denoted by m_c as shown in Fig. 4(b). We focus on the spatial resolution in Y direction since resolutions in X and Y directions become equivalent when the aperture is a D -by- D square. Consider signals at frequency f_k , the phase difference between received signal at m_1 and $(m_1 - \Delta_y)$ is approximately $\frac{D}{4\sqrt{R^2+(D/2)^2}} \frac{2\pi f_k}{c} \Delta_y$ w.r.t. a subtle distance Δ_y , corresponding to frequency $\frac{D}{\sqrt{4R^2+D^2}} f_k$. Moreover, the phase difference between received signal at $(m_c + \Delta_y)$ and m_c is 0, corresponding to frequency 0. According to Definition 1, the bandwidth in $f^{(y)}$ direction, denoted by \mathcal{B}_y is approximately

$$\mathcal{B}_y \approx 2 \times \mathbb{E}_k \left[\frac{D}{\sqrt{4R^2 + D^2}} f_k - 0 \right] = \frac{2D}{\sqrt{4R^2 + D^2}} f_c, \quad (38)$$

where $f_c = \frac{f_1 + f_K}{2}$. The azimuth resolution in Y direction can be straightforward obtained as

$$\delta_y = \frac{c}{\mathcal{B}_y} \approx \frac{c\sqrt{4R^2 + D^2}}{2f_c D}. \quad (39)$$

It is shown to be proportional to the term $\frac{\sqrt{4R^2+D^2}}{D}$, meaning that higher azimuth resolution can be achieved when the TV is closer and the aperture size becomes larger.

2) *Range Resolution:* Samplings at a fixed location $(p_m^{(x)}, p_m^{(x)}, 0)$ consist of signals at all frequencies used. Thus bandwidth in the f_z direction is $\mathcal{B}_z \approx (f_K - f_1)$, and the range resolution can be obtained as

$$\delta_z = \frac{c}{\mathcal{B}_z} \approx \frac{c}{(f_K - f_1)}, \quad (40)$$

where f_K and f_1 are maximum and minimum frequencies in the SFCW specified in (10).

Remark 9 (Sampling Requirements). To achieve the above resolutions, there exist two kinds of sampling requirements on spatial and frequency domains.

- **Spatial Sampling:** The spatial sampling represents the distance between two adjacent receive antennas. To achieve the resolution in (39), the receive antennas deployment over the “equivalent aperture” needs to meet the Nyquist sampling criterion such that the required

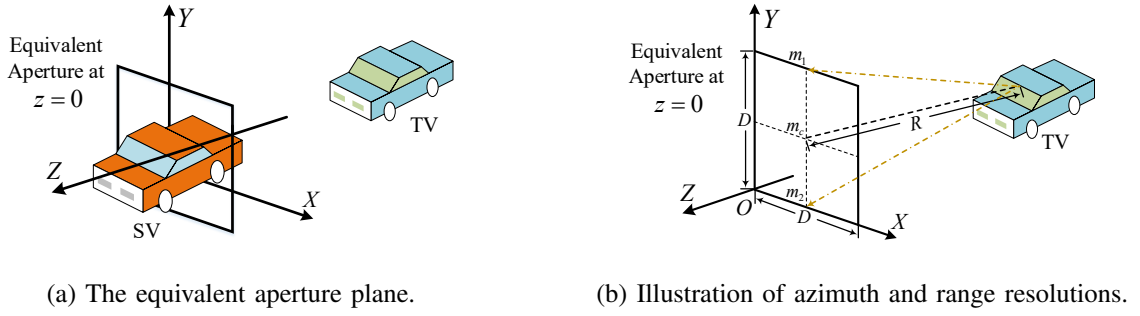


Figure 4: Illustration of azimuth and range resolutions.

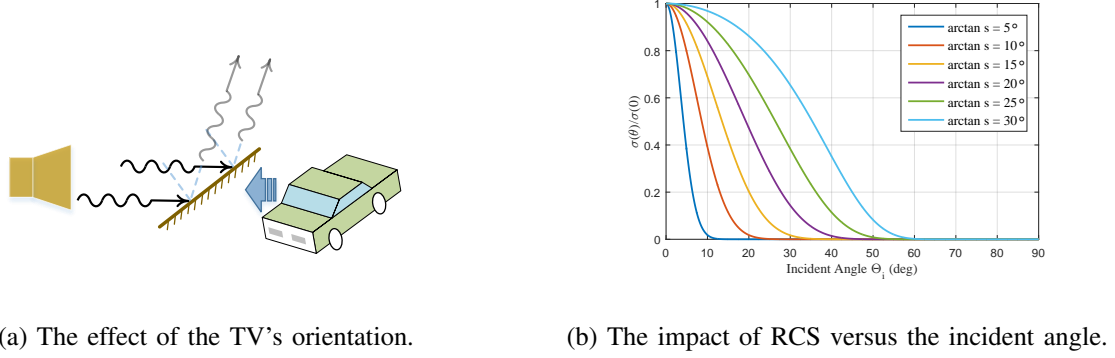


Figure 5: The effect of RCS on positioning techniques based on RADAR systems.

sampling intervals are less than Δ_x and Δ_y to avoid aliasing. Therefore, the distances between two adjacent receive antennas along X or Y directions are

$$\Delta_x = \Delta_y \leq \min_R \left\{ \frac{c}{2f_c} \frac{\sqrt{4R^2 + D^2}}{2D} \right\} \stackrel{(a)}{=} \frac{c}{4f_c}, \quad (41)$$

where (a) follows for the worst case with $R = 0$. Moreover, since the Z -axis is defined as the direction of AoA which varies over time, the distance between two adjacent receive antennas in all directions should be smaller than $\frac{c}{4f_c}$.

- **Frequency sampling:** The frequency sampling interval refers to the frequency gap Δ to achieve the maximum ranging distance R_{\max} , given the resolution δ_z (40). Specifically, the number of the minimum samples for the resolution δ_z is given as $\frac{R_{\max}}{\delta_z}$, which provides the following upper bound as

$$\frac{R_{\max}}{\delta_z} \leq \frac{f_K - f_1}{\Delta}. \quad (42)$$

Plugging (40) into (42) and with some manipulations, we have

$$\Delta \leq \frac{c}{R_{\max}}. \quad (43)$$

D. Propagation Loss Analysis

The signal propagation loss determines the power level of the received signals, so as the performance of the detected position against noise. In this subsection, we analyze the propagation loss of the proposed COMPOP and existing multi-point positioning techniques, i.e. RADAR or LIDAR, over a LoS link for signal power comparison. It is obvious that the proposed technique experiences less power loss than RADAR-based techniques due to the half propagation distance. Besides, the orientation of the target surface is another factor to affect the reflected signal power as shown in Fig. 5(a). Specifically, for RADAR-based multi-point positioning techniques, the received signal power can be expressed as

$$P_r^{(c)} = \frac{P_t G_t}{4\pi R^2} \sigma(\Theta_i) \frac{1}{4\pi R^2} A_{\text{eff}} = \frac{P_t G_t \lambda^2}{64\pi^3 R^4} \sigma(\Theta_i), \quad (44)$$

where P_t and G_t are the input power and gain of the transmit antennas, and R is the distance from the RADAR to the target. The other two factors, σ and $A_{\text{eff}} = \frac{\lambda^2}{4\pi}$ are *radar cross-section* (RCS) of the target and the effective area of the RADAR receive antenna, respectively [31]. The RCS σ is mathematically defined as

$$\sigma(\Theta_i) = \frac{|\Gamma_s(0)|^2}{2s^2} \sec^4 \Theta_i \exp \left\{ -\frac{\tan^2 \Theta_i}{s^2} \right\}, \quad (45)$$

where $\Gamma_s(0)$ is the Fresnel reflection coefficient for normal incidence for each s^2 , Θ_i is the incident angle and s^2 is a parameter measuring the roughness of the target surface [32]. The RCS is uncontrollable in the RADAR system design. From (44) and (45), the impact of the target's surface orientation, related to the incident angle Θ_i , is shown clearly. Fig. 5(b) indicates that the received signal power $P_r^{(c)}$ degrades seriously when the incident angle is large.

On the other hand, according to (44), the received signal power of our proposed technique can be expressed as $P_r = \frac{P_t G_t \lambda^2}{(4\pi R)^2}$, where the RCS has no influence on the received signal power of our proposed COMPOP since the transmit antennas are isotropic. Moreover, reducing the signal propagation distance to half brings a power gain of $4\pi R^2$. Therefore, the proposed COMPOP is able to function well regardless the orientation of the TV and guarantee a signal power gain compared with conventional RADAR systems.

IV. COMPOP USING SURFACE REFLECTION IN NLOS

Consider a NLoS scenario where the TV's LoS path to the SV is blocked but several NLoS paths reflected by nearby vehicles are available. We exploit mmWave spectrum's specular

signal reflection on the smooth surfaces of nearby vehicles², establishing mirror-reflection links between the TV and the SV. Based on signals reflected from different paths, given as (16), multiple virtual vehicles symmetric to the actual TV concerning the reflection surfaces can be detected via LoS COMPOP. Since SV has no prior information of the reflection surfaces, an additional step should be required to combine multiple virtual TVs into the actual one. To this end, we design a two-stage approach following 1) LoS COMPOP and 2) virtual TV combining, as illustrated in Fig. 6.

Additional assumptions used in this section are summarized for clarification in the sequel:

- **Specular Reflection:** The surfaces of nearby vehicles or buildings are able to provide specular reflections for mmWave signals as mentioned above.
- **Reflection Surfaces Vertical to the Ground:** We consider the case where the reflection surfaces are vertical to the ground, which is common in practice. This assumption can be easily relaxed as illustrated in Remark 12 later.

A. LoS COMPOP

Firstly, we assume that the signals reflected from different paths can be perfectly resolved at the SV by the AoA differentiation. Then based on signals received from each path, the LoS COMPOP can be accomplished by the following two steps.

1) *Synchronization:* The operation is similar to the synchronization under LoS in Sec. III-A. Consider the signals from path ℓ as an example. Let σ denote the system clock difference satisfying the following equations:

$$\sigma = \tau_{a,m}^{(\ell)} - \frac{\eta_{a,m}^{(\ell)}}{2\pi\Delta} = \tau_{b,m}^{(\ell)} - \frac{\eta_{b,m}^{(\ell)}}{2\pi\Delta}, \quad (46)$$

where $\{\tau_{a,m}^{(\ell)}, \tau_{b,m}^{(\ell)}\}$ and $\{\eta_{a,m}^{(\ell)}, \eta_{b,m}^{(\ell)}\}$ represent the propagation time and phase difference of the signature waveforms from the antennas a and b through ℓ -th mirror-reflection link, respectively. Following the procedures in Sec. III-A gives the locations of antennas a and b on the virtual TV ℓ , denoted by $\mathbf{x}_a^{(\ell)}$ and $\mathbf{x}_b^{(\ell)}$, which are different from the real locations \mathbf{x}_a and \mathbf{x}_b . As in the case with an LoS path, the points $\mathbf{x}_a^{(\ell)}$ and $\mathbf{x}_b^{(\ell)}$ are used to compensate the system clock difference, which enables virtual vehicle positioning in Sec. IV-A2. Besides, $\mathbf{x}_a^{(\ell)}$ and $\mathbf{x}_b^{(\ell)}$ help estimate the reflection surface elaborated in Sec. IV-B2.

²MmWave spectrum has two reflection properties on vehicles' metal surfaces, where 1) its reflection coefficient is almost 1 unless the incident angle is near $\frac{\pi}{2}$ or 0, and 2) mmWave signals experience the mirror-like specular reflection [33].

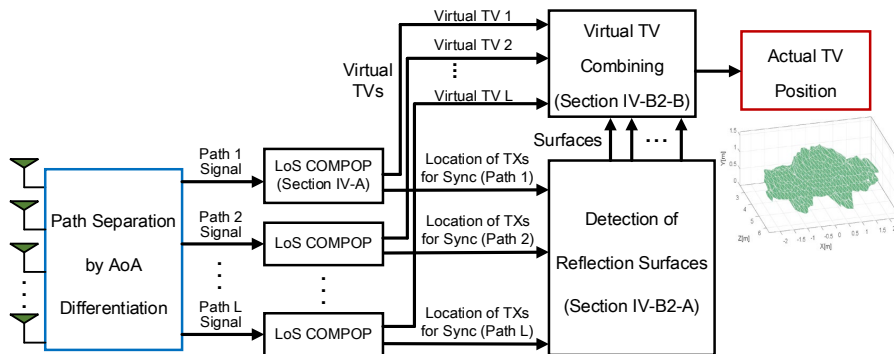


Figure 6: Diagram of COMPOP in NLoS.

Remark 10 (TV Recognition in NLoS). Considering that multiple reflection links exist for the same TV in NLoS case, the detected system clock difference can help recognize the TVs. Specifically, signature waveforms transmitted from the same TV share the same system clock difference σ regardless of different signal paths, since they are originated from the same TV. Therefore, the SV can recognize signals from the same TV or different TVs according to the detected system clock difference $\tilde{\sigma}$.

2) *Virtual TV Positioning*: Recall that plugging the perfectly estimated σ into the demodulated signal (16) gives the following 3D surface integral form of $y_m^{\ell,k}$ as

$$y_m^{\ell,k} = y^{(\ell)}(\mathbf{p}_m, f_k) = \Gamma^{(\ell)} \int_{\mathbb{R}^3} \mathbb{1}_{\{\mathbf{x}^{(\ell)} \in \mathcal{X}^{(\ell)}\}} \exp\left(-j \frac{2\pi f_k}{c} D^{(\ell)}(\mathbf{x}, \mathbf{p}_m)\right) d\mathbf{x}^{(\ell)}, \quad (47)$$

where $y^{(\ell)}(\mathbf{x}, f) : \mathbb{R}^4 \rightarrow \mathbb{R}$ is a continuous function, and $D^{(\ell)}(\mathbf{x}, \mathbf{p}_m)$ represents the Euclidean distance from point $\mathbf{x}^{(\ell)}$ in $\mathcal{X}^{(\ell)}$, which is symmetric to point \mathbf{x} in \mathcal{X} w.r.t. the ℓ -th reflection surface, to the location of the SV's antenna m denoted by $\mathbf{p}_m = (p_m^{(x)}, p_m^{(y)}, p_m^{(z)})^T$. Compared with (28) in the LoS scenario, the reflection coefficient $\Gamma^{(\ell)}$ can be considered as a constant scaling factor, which does not affect the positioning procedure. Following the same steps in Sec. III-B, the virtual TV ℓ 's power spectrum $\Phi[\mathbf{x}^{(\ell)}]$ can be calculated. After the peak detection in (36), we can obtain the virtual locations of the transmit antennas $\mathcal{X}^{(\ell)}$, which is referred to as virtual TV ℓ . The estimated virtual TVs are used to position the actual TV explained in Sec. IV-B2.

B. Virtual TV Combining

1) *Overview*: This subsection aims at positioning the actual TV with multiple virtual TVs detected in Sec. IV-A2 under the assumption that the reflection surfaces are vertical to the

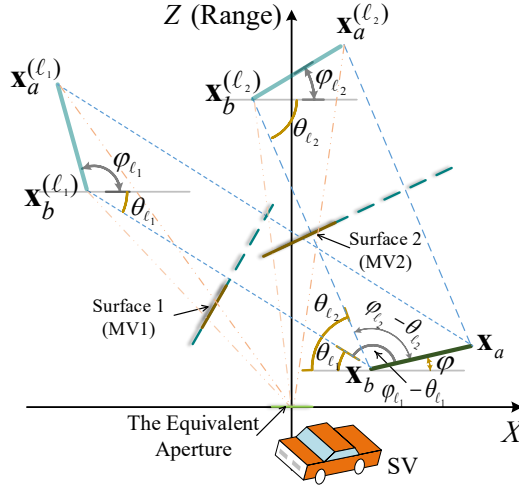


Figure 7: Geometric relations between the virtual and actual TVs from the top view.

ground, which is common in practice. Since the actual TV can be directly obtained by shifting the virtual TVs w.r.t. their corresponding reflection surfaces, the key step becomes the detection of the reflection surfaces. To this end, an algorithm to position the actual TV, consists of two steps: 1) detection of reflection surfaces; and 2) combining virtual TVs. The detailed procedures are illustrated in the following.

2) *Algorithm Description:*

- *A. Detection of Reflection Surfaces:* Consider the virtual locations of representative transmit antennas a and b detected in Sec. IV-A1 with coordinates $\mathbf{x}_a^{(\ell)} = (x_a^{(\ell)}, y_a^{(\ell)}, z_a^{(\ell)})^T$ and $\mathbf{x}_b^{(\ell)} = (x_b^{(\ell)}, y_b^{(\ell)}, z_b^{(\ell)})^T$, which are symmetric to the counterpart points on the actual TV denoted by $\mathbf{x}_a = (x_a, y_a, z_a)^T$ and $\mathbf{x}_b = (x_b, y_b, z_b)^T$ w.r.t. the reflection surface ℓ . It can be inferred from Fig. 7 that given the locations $(\mathbf{x}_a^{(\ell)}, \mathbf{x}_b^{(\ell)})$, the reflection surfaces can be straightforwardly obtained if $(\mathbf{x}_a, \mathbf{x}_b)$ is estimated. Therefore, the problem is translated into the detection of representative transmit antennas $(\mathbf{x}_a, \mathbf{x}_b)$. To this end, we summarize the geometric relation between $(\mathbf{x}_a^{(\ell)}, \mathbf{x}_b^{(\ell)})$ and $(\mathbf{x}_a, \mathbf{x}_b)$ in the following lemma.

Lemma 2. Consider virtual TVs ℓ_1 and ℓ_2 whose representative points are $\{\mathbf{x}_a^{(\ell_1)}, \mathbf{x}_b^{(\ell_1)}\}$ and $\{\mathbf{x}_a^{(\ell_2)}, \mathbf{x}_b^{(\ell_2)}\}$ respectively, which have geometric relations with the counterpart points on the actual TV denoted by $(\mathbf{x}_a, \mathbf{x}_b)$ as follows.

- 1) Let θ_ℓ denote the directed angle from the X -axis (parallel to the ground) to the line between $\mathbf{x}_a^{(\ell)}$ and \mathbf{x}_a or $\mathbf{x}_b^{(\ell)}$ and \mathbf{x}_b (see Fig. 7). According to the geometric relation

illustrated in Fig. 7, \mathbf{x}_a can be given in terms of θ_{ℓ_1} and θ_{ℓ_2} as

$$\mathbf{x}_a = \begin{pmatrix} x_a \\ y_a \\ z_a \end{pmatrix} = \begin{pmatrix} \frac{(z_a^{(\ell_1)} - z_a^{(\ell_2)}) + (x_a^{(\ell_2)} \tan(\theta_{\ell_2}) - x_a^{(\ell_1)} \tan(\theta_{\ell_1}))}{\tan(\theta_{\ell_2}) - \tan(\theta_{\ell_1})} \\ y_a^{(\ell_1)} \text{ or } y_a^{(\ell_2)} \\ z_a^{(\ell_1)} + \tan(\theta_{\ell_1})(x_a - x_a^{(\ell_1)}) \end{pmatrix}, \quad (48)$$

and similarly the expression of \mathbf{x}_b in terms of θ_{ℓ_1} and θ_{ℓ_2} is obtained by replacing all a in (48) with b .

- 2) Let φ_ℓ denote the directed angle from the X -axis to the line segment of virtual TV ℓ , from $\mathbf{x}_a^{(\ell)}$ to $\mathbf{x}_b^{(\ell)}$, as shown in Fig. 7. The angles θ_ℓ and φ_ℓ of two virtual TVs ℓ_1 and ℓ_2 follows the relation

$$\theta_{\ell_1} - \theta_{\ell_2} = \frac{\varphi_{\ell_1} - \varphi_{\ell_2}}{2}. \quad (49)$$

Proof: Please refer to Appendix C. □

Based on Lemma 2, the representative points ($\mathbf{x}_a, \mathbf{x}_b$) are estimated as follows. First, all angles $\{\theta_\ell\}_{\ell=2}^L$ can be expressed in terms of θ_1 as $\theta_\ell = \theta_1 + \frac{\varphi_\ell - \varphi_1}{2}$ using (49). Next, plugging each pair of (θ_1, θ_ℓ) into (48) makes it possible to express the locations a and b w.r.t θ_1 , denoted by $(\mathbf{v}_a^{(\ell)}(\theta_1), \mathbf{v}_b^{(\ell)}(\theta_1))$. If θ_1 is correct, $(\mathbf{v}_a^{(\ell)}(\theta_1), \mathbf{v}_b^{(\ell)}(\theta_1))$ naturally coincides with $(\mathbf{x}_a, \mathbf{x}_b)$. In other words, estimating $(\mathbf{x}_a, \mathbf{x}_b)$ is translated into finding θ_1 minimizing the following squared Euclidean distance as

$$\theta_1^* = \arg \min_{\theta_1} \sum_{\ell_1=2}^L \sum_{\ell_2=2}^L \left(\left\| \mathbf{v}_a^{(\ell_1)}(\theta_1) - \mathbf{v}_a^{(\ell_2)}(\theta_1) \right\|_2 + \left\| \mathbf{v}_b^{(\ell_1)}(\theta_1) - \mathbf{v}_b^{(\ell_2)}(\theta_1) \right\|_2 \right). \quad (50)$$

The optimal θ_1^* is computed by 1D search over $[-\pi, \pi]$, and the resultant $\mathbf{x}_a^* = \frac{1}{L-1} \sum_{\ell=2}^L \mathbf{v}_a^{(\ell)}(\theta_1^*)$ and $\mathbf{x}_b^* = \frac{1}{L-1} \sum_{\ell=2}^L \mathbf{v}_b^{(\ell)}(\theta_1^*)$ can be directly obtained by using the optimal θ_1^* . Then with $(\mathbf{x}_a^*, \mathbf{x}_b^*)$, the reflection surface ℓ , which is located on the middle of \mathbf{x}_a^* and \mathbf{x}_b^* , can be expressed by a line because it is perpendicular to $X - Z$ plane such that

$$z = -\frac{1}{\tan(\theta_\ell^*)} \left(x - \frac{x_a^{(\ell)} + x_a^*}{2} \right) + \frac{(z_a^{(\ell)} + z_a^*)}{2}, \quad (51)$$

where $\mathbf{x}_a^* = (x_a^*, y_a^*, z_a^*)^T$, and $\theta_\ell^* = \theta_1^* + \frac{\varphi_\ell - \varphi_1}{2}$.

Proposition 3 (Feasibility Condition for NLoS Position Combining). To detect the actual TV in NLoS, at least three reflection surfaces are required: $L \geq 3$.

Proof: Please refer to Appendix D. □

- *B. Combining Virtual TVs:* With the knowledge of the reflection surfaces, the actual TV \mathcal{X} can be obtained as elaborated in the following proposition.

Proposition 4 (Position Combining). Consider the virtual TV ℓ represented by $\mathcal{X}^{(\ell)}$. Given θ_ℓ^* and \mathbf{x}_a^* (or \mathbf{x}_b^*), the actual TV \mathcal{X} can be obtained by the following mapping function:

$$\mathcal{X} = \mathbf{G}(\mathcal{X}^{(\ell)}) \quad (52)$$

where

$$\mathbf{G}(\mathbf{x}^{(\ell)}) = (x^*, y^*, z^*)^T = \begin{pmatrix} x^{(\ell)} + \frac{\tan(\theta_\ell^*)}{1 + \tan^2(\theta_\ell^*)} \left(\frac{x_a^{(\ell)} + x_a^*}{\tan(\theta_\ell^*)} + z_a^{(\ell)} + z_a^* - \frac{2x^{(\ell)}}{\tan(\theta_\ell^*)} - 2z^{(\ell)} \right) \\ y^{(\ell)} \\ z^{(\ell)} + \frac{\tan^2(\theta_\ell^*)}{1 + \tan^2(\theta_\ell^*)} \left(\frac{x_a^{(\ell)} + x_a^*}{\tan(\theta_\ell^*)} + z_a^{(\ell)} + z_a^* - \frac{2x^{(\ell)}}{\tan(\theta_\ell^*)} - 2z^{(\ell)} \right) \end{pmatrix}, \quad \mathbf{x}^{(\ell)} \in \mathbb{R}^3$$

Proof: Please refer to Appendix E. □

Remark 11 (Existence of LoS path). The LoS case is a special realization of the NLoS case, where one couple of representative points $(\mathbf{x}_a^{\text{LoS}}, \mathbf{x}_b^{\text{LoS}})$ are equivalent to the exact location $(\mathbf{x}_a, \mathbf{x}_b)$. Therefore, all mathematical expressions for the virtual TV combining still hold when the LoS link exists, and the resultant $(\mathbf{x}_a^*, \mathbf{x}_b^*)$ can be obtained in the same way.

Remark 12 (Arbitrary Reflection Surfaces). The assumption that all reflection surfaces are vertical to the ground can be easily relaxed with one more antenna transmitting signature waveform s_c . In this case, representative points $\{\mathbf{x}_a^\ell, \mathbf{x}_b^\ell, \mathbf{x}_c^\ell | \forall \ell\}$ are detected in the clock synchronization step. Analogous to the result in (51), reflection surfaces can then be located, without the assumption, by exploiting the information of these representative points, so as the actual TV position.

C. Propagation Loss Analysis

Similar to the analysis in Sec. III-D, we also give signal power comparison between the proposed COMPOP and traditional RADAR techniques over the reflection links. Although RADAR techniques do not provide solutions to positioning without a LoS, we still provide the received signal power of a reflection link, say the ℓ -th reflection link, as

$$P_r^{(c)} = \frac{P_t G_t \lambda^2}{4^5 \pi^5 R^8} \sigma(\Theta_i) \sigma^2(\Theta_i^{(\ell)}), \quad (53)$$

where $\Theta_i^{(\ell)}$ is the incident angle on the reflection surface ℓ . For the proposed COMPOP, signals from each reflection link give one virtual TV detected with algorithm in Sec. IV-A2. For the reflection link ℓ , the received signal power is

$$P_r^{(\ell)} = \frac{P_t G_t \lambda^2}{64\pi^3 (R_1^{(\ell)})^2 (R_2^{(\ell)})^2} \sigma(\Theta_i^{(\ell)}), \quad (54)$$

where $R_1^{(\ell)}$ is the distance from the transmit antenna to the reflection surface ℓ , and $R_2^{(\ell)}$ is the distance from the receiver to the reflection surface ℓ . It is obvious that the proposed COMPOP achieves a much lower propagation loss than the conventional RADAR techniques.

V. SIMULATION RESULTS

In this section, the performance of the proposed COMPOP technique is evaluated by realistic settings. Signature waveforms at 4 frequencies are used for the synchronization procedure. The number of frequencies used in the SFCW (10) is $K = 256$ ranging from 57 GHz to 60 GHz with the constant gap $\Delta = 11.72$ MHz. The four frequencies used in the signature waveforms (1) are $(57 - \Delta \cdot i)$ GHz where $i = 1, 2, 3, 4$. The numbers of the TV's and SV's antennas are $N_t = N_r = 200$, which are uniformly deployed on the vehicles bodies. The size of the equivalent receive aperture is 1×1 m². The SNR of each received signal is fixed to 10 dB. The number of reflection surfaces are 3 and the distance between TV and SV is 8 m unless stated otherwise.

For the performance metric, we use the Hausdorff distances defined as follows.

Definition 1 (Hausdorff distance [34]). The Hausdorff distance is widely used to evaluate the image retrieval performance by measuring the similarity between two images. Consider an image \mathcal{A} and its retrieved one \mathcal{B} , both of which are composed of discrete points. The Hausdorff distance is defined as

$$H(\mathcal{A}, \mathcal{B}) = \max(h(\mathcal{A}, \mathcal{B}), h(\mathcal{B}, \mathcal{A})), \quad (55)$$

where $h(\mathcal{A}, \mathcal{B}) = \max_{a \in \mathcal{A}} \min_{b \in \mathcal{B}} \|a - b\|$.

A. Graphical Example of Multi-Point Positioning

This subsection aims at explaining the entire vehicular positioning procedure with step-by-step graphical examples. To this end, we consider the topology with three reflection surfaces illustrated in Fig. 8. The TV is represented by discrete points, each of which is one TV's antenna. The size of the TV is $3 \times 1 \times 0.6$ m³. The equivalent receive aperture is parallel to Y -axis and

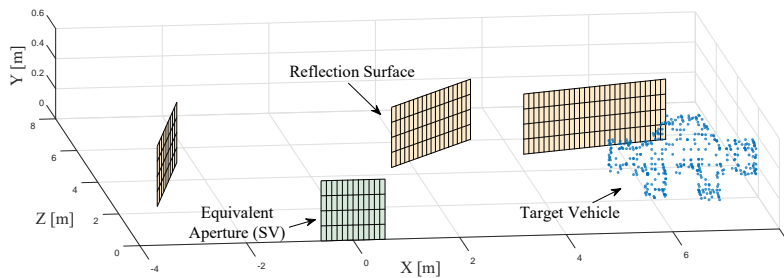


Figure 8: Initial topology.

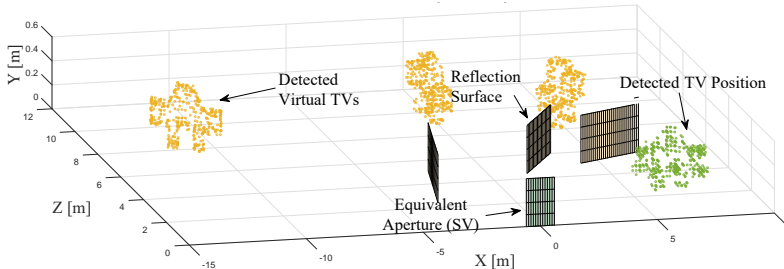


Figure 9: The detection of the virtual TVs.

located at $(0, 0, 0)$. The equations of three reflection surfaces are given as $z = 1.02x + 3$, $z = \frac{x+13}{4}$, and $z = 3x + 4$.

Using the reflection surfaces, the SV detects three virtual TVs represented by yellow slots in Fig. 9, each of which is differentiable using AoA information. By the intelligent combining algorithm in Proposition 4, each virtual TV can be shifted to its real location represented by green spots, of which the Hausdorff distance is 0.355m, which is relatively small compared to the size of the TV. After graphical rendering process, the final detected position is obtained as in Fig. 10(b) that is similar to the original one in Fig. 10(a).

B. Error in Clock Synchronization

The clock difference detection error is omitted in procedures after clock synchronization according to the analysis in Proposition 2. To justify such an assumption, we check it by simulations given in Fig. 12. It clearly shows that the clock difference detection error can be well suppressed by an appropriate number of antennas, e.g., $N_r = 16$ or $N_r = 64$, at the receiver. Therefore, it is reasonable to assume perfect clock synchronization for convenience.

C. Different Interpolation Methods

The performance by using different interpolation methods for resampling in Sec. III-B is also checked by simulations in Fig. 11. It can be observed that all interpolation methods gives

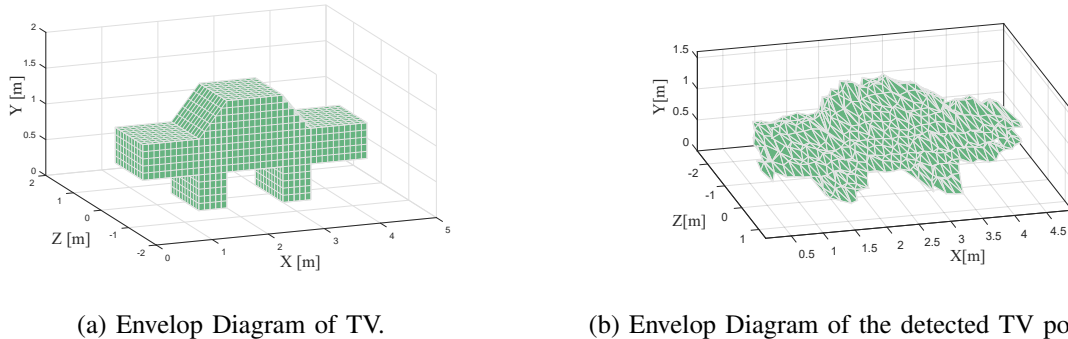


Figure 10: The envelop digaram comparison of the TV model and the detected position.

similar performance, where the errors are negligible for vehicular positioning. Therefore, we simply adopt linear interpolation in this work for low complexity.

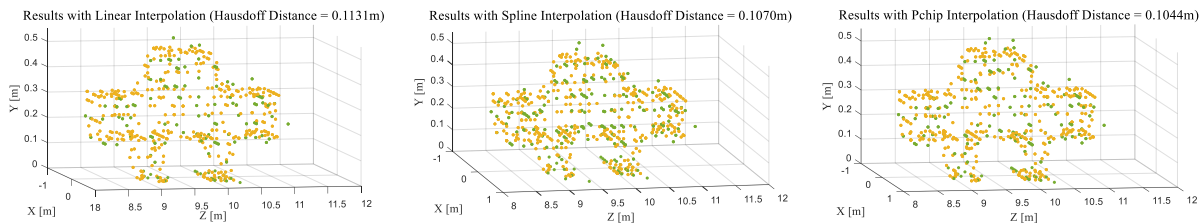


Figure 11: Comparison between different interpolation methods, where the initial TV model is in yellow, and the retrieved TV position by algorithm in Sec. III-B is in green.

D. Effect of Distance between SV and TV

In Fig. 13, the Hausdorff distances are given under different TV-SV distances, showing that the positioning quality is degraded as the distance between the TV and SV increases. This phenomenon can be explained by (39), where the spatial resolution becomes poor when the detection range R is large. Therefore, the SV may not be able to capture the clear position of the TVs far away, especially when the number of reflection surfaces is small. Moreover, the relation between the Hausdorff distance and the TV-SV distance is not linear, which is led by the $\tan(\cdot)$ function in the solution (48). With noise in consideration, the Hausdorff distance, indicating the comprehensive error level, increases faster when the TV-SV distance becomes larger.

E. Effect of Reflection Surface Number

The relation between the performance and the number of reflection surfaces is also presented in Fig. 13 (a). As explained in Sec. IV-B, signals reflected from any three reflection surfaces

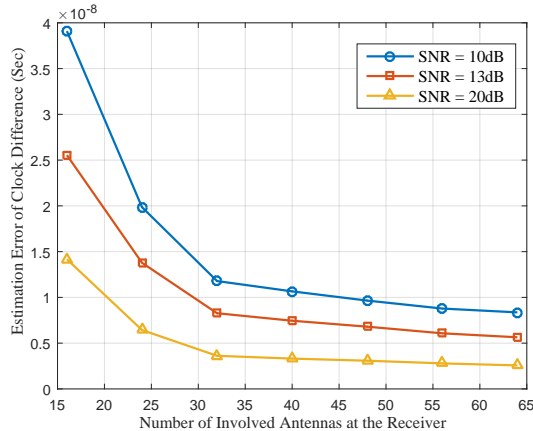
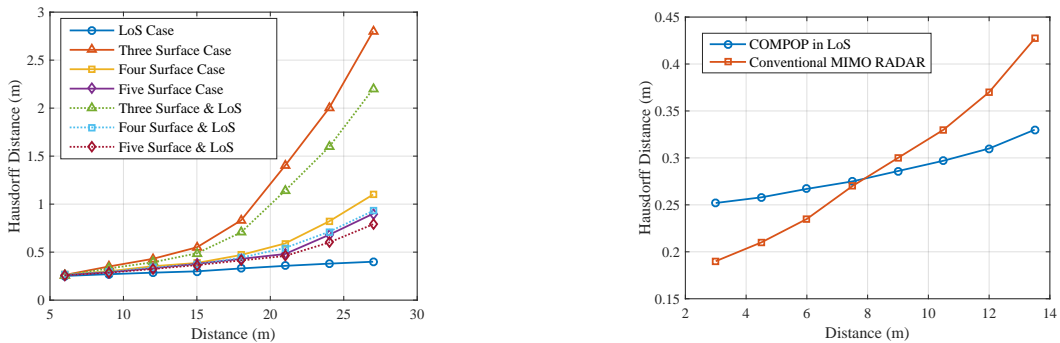


Figure 12: Estimation error of the clock difference versus the number of antennas involved at the receiver.



(a) The performance of the COMPOP with reflection links. (b) Comparison between the COMPOP and the existing MIMO RADAR.

Figure 13: The performance of the proposed COMPOP versus distance.

give one estimation of θ_1 , but the resultant positioning quality is low due to the phase error, and the performance becomes unstable when the TV-SV distance increases. We also consider the cases where more than 3 reflection links exist ($L > 3$). Larger L provides more combinations to estimate θ_1 , resulting in more accurate estimation of θ_1 by canceling out individual estimated error. Moreover, the LoS case leads to the minimum Hausdorff distance. It is considered as a lower bound because the operation in Sec. IV-B is not involved, and the estimation error only comes from the approach in Sec. III-B. The case with mixed LoS and NLoS paths are also investigated here, which is plotted by dotted lines. It can be observed that although the existence of LoS path enhances the performance, the errors from NLoS paths hamper the accuracy.

F. Comparison to MIMO RADAR

The performance of conventional MIMO RADAR [12], [15] is also checked by simulations as shown in Fig. 13 (b), which is considered as a baseline of the proposed COMPOP design. The conventional MIMO RADAR is naturally synchronized with co-located transceivers and thus free from the clock difference detection error. Hence, conventional MIMO RADAR could be a better choice in short distance. However, when the distance becomes larger, the proposed COMPOP has a signal power gain and thus shows better performance as illustrated in Sec. III-D.

VI. CONCLUSION

In this paper, a novel *Cooperative Multi-point Positioning* (COMPOP) approach via mmWave signal transmissions has been proposed to capture the shape and location information of the TVs in both LoS and NLoS. The cooperative transmission between the TV and SV enables the real-time COMPOP without scanning process. The synchronization issue due to transceiver separation has been well addressed by a PDoA-based positioning approach. In NLoS case, COMPOP establishes mirror-reflection links between the TV and SV under the assistance of the nearby vehicles. The geometric relation between the virtual and actual TVs has been exploited to position the actual TV via an intelligent combining algorithm without priori knowledge on the nearby vehicles. In conclusion, the proposed COMPOP is available in both LoS and NLoS situations with ultra-low latency and high detection accuracy, which is challenging for existing vehicular sensing techniques (e.g., RADAR and LIDAR). Therefore, this technique opens a new area of mmWave-based vehicular positioning and sensing. We believe the proposed COMPOP contributes to more intelligent and safer autonomous driving, and the potential of mmWave-based vehicular sensing can still be activated in the future.

APPENDIX

A. Proof of proposition 2

Due to the assumption of Gaussian phase error, the covariance of the location estimation can be expressed as

$$\text{cov}(\tilde{\mathbf{x}}_a) = \mathbf{X}\sigma_z^2\mathbf{I}_3, \quad (56)$$

where \mathbf{X} is a 3-by-3 matrix as

$$\mathbf{X} = \left(\mathbf{G}(\tilde{\mathbf{x}}_a)^T \mathbf{G}(\tilde{\mathbf{x}}_a) \right)^{-1}$$

$$\begin{aligned}
&= \left(\sum_{m=2}^{N_r} \begin{bmatrix} \left(\frac{\partial F_m(\tilde{\mathbf{x}}_a)}{\partial x_a} \right)^2 & \frac{\partial F_m(\tilde{\mathbf{x}}_a)}{\partial x_a} \frac{\partial F_m(\tilde{\mathbf{x}}_a)}{\partial y_a} & \frac{\partial F_m(\tilde{\mathbf{x}}_a)}{\partial x_a} \frac{\partial F_m(\tilde{\mathbf{x}}_a)}{\partial z_a} \\ \frac{\partial F_m(\tilde{\mathbf{x}}_a)}{\partial x_a} \frac{\partial F_m(\tilde{\mathbf{x}}_a)}{\partial y_a} & \left(\frac{\partial F_m(\tilde{\mathbf{x}}_a)}{\partial y_a} \right)^2 & \frac{\partial F_m(\tilde{\mathbf{x}}_a)}{\partial y_a} \frac{\partial F_m(\tilde{\mathbf{x}}_a)}{\partial z_a} \\ \frac{\partial F_m(\tilde{\mathbf{x}}_a)}{\partial x_a} \frac{\partial F_m(\tilde{\mathbf{x}}_a)}{\partial z_a} & \frac{\partial F_m(\tilde{\mathbf{x}}_a)}{\partial y_a} \frac{\partial F_m(\tilde{\mathbf{x}}_a)}{\partial z_a} & \left(\frac{\partial F_m(\tilde{\mathbf{x}}_a)}{\partial z_a} \right)^2 \end{bmatrix} \right)^{-1} \\
&= \frac{1}{N_r - 1} \left(\frac{1}{N_r - 1} \sum_{m=2}^{N_r} \begin{bmatrix} \left(\frac{\partial F_m(\tilde{\mathbf{x}}_a)}{\partial x_a} \right)^2 & \frac{\partial F_m(\tilde{\mathbf{x}}_a)}{\partial x_a} \frac{\partial F_m(\tilde{\mathbf{x}}_a)}{\partial y_a} & \frac{\partial F_m(\tilde{\mathbf{x}}_a)}{\partial x_a} \frac{\partial F_m(\tilde{\mathbf{x}}_a)}{\partial z_a} \\ \frac{\partial F_m(\tilde{\mathbf{x}}_a)}{\partial x_a} \frac{\partial F_m(\tilde{\mathbf{x}}_a)}{\partial y_a} & \left(\frac{\partial F_m(\tilde{\mathbf{x}}_a)}{\partial y_a} \right)^2 & \frac{\partial F_m(\tilde{\mathbf{x}}_a)}{\partial y_a} \frac{\partial F_m(\tilde{\mathbf{x}}_a)}{\partial z_a} \\ \frac{\partial F_m(\tilde{\mathbf{x}}_a)}{\partial x_a} \frac{\partial F_m(\tilde{\mathbf{x}}_a)}{\partial z_a} & \frac{\partial F_m(\tilde{\mathbf{x}}_a)}{\partial y_a} \frac{\partial F_m(\tilde{\mathbf{x}}_a)}{\partial z_a} & \left(\frac{\partial F_m(\tilde{\mathbf{x}}_a)}{\partial z_a} \right)^2 \end{bmatrix} \right)^{-1}, \quad (57)
\end{aligned}$$

where the inverse matrix's each component converges to its expectation as N_r becomes large, which becomes independent to N_r . In other words, \mathbf{X} is proportional to $\frac{1}{N_r - 1}$.

B. Proof of Lemma 1

We adopt the scalar diffraction idea in [29] that the wave field can be decomposed as an infinite integral of planar waves, given as

$$\exp\left(-j\frac{2\pi f}{c}D(\mathbf{x}, \mathbf{p}_m)\right) = \iint_{f(z)=\sqrt{f^2-(f(x))^2-(f(y))^2}} \exp\left(-j\frac{2\pi}{c}\mathbf{f}^T(\mathbf{x} - \mathbf{p}_m)\right) df^{(x)}df^{(y)}, \quad (58)$$

where $\mathbf{f} = [f^{(x)}, f^{(y)}, f^{(z)}]^T$ denotes a spatial frequency vector. Accordingly, the signal in (28) can be expanded by rewriting the exponential term in terms of \mathbf{f} as

$$\begin{aligned}
y(\mathbf{p}_m, f) &= \int_{\mathbb{R}^3} \mathbb{1}_{\{\mathbf{x} \in \mathcal{X}\}} \left\{ \iint_{f(z)=\sqrt{f^2-(f(x))^2-(f(y))^2}} \exp\left(-j\frac{2\pi}{c}\mathbf{f}^T(\mathbf{x} - \mathbf{p}_m)\right) df^{(x)}df^{(y)} \right\} d\mathbf{x} \\
&= \iint_{f(z)=\sqrt{f^2-(f(x))^2-(f(y))^2}} \left\{ \int_{\mathbb{R}^3} \mathbb{1}_{\{\mathbf{x} \in \mathcal{X}\}} \exp\left(-j\frac{2\pi}{c}\mathbf{f}^T(\mathbf{x} - \mathbf{p}_m)\right) d\mathbf{x} \right\} df^{(x)}df^{(y)} \\
&= \iint_{f(z)=\sqrt{f^2-(f(x))^2-(f(y))^2}} \underbrace{\left\{ \int_{\mathbb{R}^3} \mathbb{1}_{\{\mathbf{x} \in \mathcal{X}\}} \exp\left(-j\frac{2\pi}{c}\mathbf{f}^T\mathbf{x}\right) d\mathbf{x} \right\}}_{\text{FT}_{3D}(\mathbb{1}_{\{\mathbf{x} \in \mathcal{X}\}})} \exp\left(j\frac{2\pi}{c}\mathbf{f}^T\mathbf{p}_m\right) df^{(x)}df^{(y)},
\end{aligned}$$

Then consider the received signal at the 2D plane $z = 0$ where $\mathbf{p}_m = (p_m^{(x)}, p_m^{(y)}, 0)^T$, given as

$$\begin{aligned}
y(p_m^{(x)}, p_m^{(y)}, 0, f) &= \iint \left\{ \text{FT}_{3D}(\mathbb{1}_{\{\mathbf{x} \in \mathcal{X}\}}) \Big|_{f(z)=\sqrt{f^2-(f(x))^2-(f(y))^2}} \right\} \exp\left(j\frac{2\pi}{c}\mathbf{f}^T\mathbf{p}_m\right) df^{(x)}df^{(y)} \\
&= \text{FT}_{2D}^{-1} \left\{ \text{FT}_{3D}(\mathbb{1}_{\{\mathbf{x} \in \mathcal{X}\}}) \Big|_{f(z)=\sqrt{f^2-(f(x))^2-(f(y))^2}} \right\}. \quad (59)
\end{aligned}$$

This finishes the proof.

C. Proof of Lemma 2

In Fig. 7, we have $\theta_{\ell_1} \in [-\pi, \pi]$ and the equations of line $l_{\mathbf{x}_a^{(\ell_1)} \mathbf{x}_a}$ and $l_{\mathbf{x}_a^{(\ell_2)} \mathbf{x}_a}$ are

$$l_{\mathbf{x}_a^{(\ell_1)} \mathbf{x}_a} : z = z_a^{(\ell_1)} + \tan(\theta_{\ell_1})(x - x_a^{(\ell_1)}); \quad l_{\mathbf{x}_a^{(\ell_2)} \mathbf{x}_a} : z = z_a^{(\ell_2)} + \tan(\theta_{\ell_2})(x - x_a^{(\ell_2)}).$$

Thus the intersection point can be solved as

$$\begin{cases} x_a = \frac{(z_a^{(\ell_1)} - z_a^{(\ell_2)}) + (x_a^{(\ell_2)} \tan(\theta_{\ell_2}) - x_a^{(\ell_1)} \tan(\theta_{\ell_1}))}{\tan(\theta_{\ell_2}) - \tan(\theta_{\ell_1})} \\ z_a = z_a^{(\ell_1)} + \tan(\theta_{\ell_1})(x_a - x_a^{(\ell_1)}) \end{cases}. \quad (60)$$

The general relations in (48) can be derived similarly. Due to the symmetric relation between the virtual and actual TVs, we have

$$\pi - \varphi = \varphi_{\ell_1} - 2\theta_{\ell_1} = \varphi_{\ell_2} - 2\theta_{\ell_2}, \quad (61)$$

D. Proof of Proposition 3

Bring (61) into (60), x_a can be simplified as

$$x_a = \frac{(z_a^{(\ell_1)} - z_a^{(\ell_2)}) + x_a^{(\ell_2)} \tan\left(\theta_{\ell_1} - \frac{\varphi_{\ell_1} - \varphi_{\ell_2}}{2}\right) - x_a^{(\ell_1)} \tan(\theta_{\ell_1})}{\tan\left(\theta_{\ell_1} - \frac{\varphi_{\ell_1} - \varphi_{\ell_2}}{2}\right) - \tan(\theta_{\ell_1})}, \quad (62)$$

which indicates that x_a is only determined by the angle $\theta_{\ell_1} \in [-\pi, \pi]$. Given the angle θ_{ℓ_1} , the estimation of x_a from (62) is denoted as \hat{x}_a . Similarly, another estimation of x_1 can be obtained from the common points $(\mathbf{x}_a^{(\ell_1)}, \mathbf{x}_b^{(\ell_1)})$ and $(\mathbf{x}_a^{(\ell_3)}, \mathbf{x}_b^{(\ell_3)})$, which is given as

$$x_a = \frac{(z_a^{(\ell_1)} - z_a^{(\ell_3)}) + x_a^{(\ell_3)} \tan\left(\theta_{\ell_1} - \frac{\varphi_{\ell_1} - \varphi_{\ell_3}}{2}\right) - x_a^{(\ell_1)} \tan(\theta_{\ell_1})}{\tan\left(\theta_{\ell_1} - \frac{\varphi_{\ell_1} - \varphi_{\ell_3}}{2}\right) - \tan(\theta_{\ell_1})}. \quad (63)$$

The estimation of x_a from (63) is denoted as \tilde{x}_a , and it can be observed from (63) that \tilde{x}_a is also only determined by θ_{ℓ_1} . Therefore, the SV can search θ_{ℓ_1} in the range of $[-\pi, \pi]$ to minimize $|\hat{x}_a - \tilde{x}_a|$. Two solutions can be obtained with the optimal θ_{ℓ_1} , denoted as \hat{x}_a^* and \tilde{x}_a^* . Then the optimal solution of x_a is given as $x_a^* = \frac{\hat{x}_a^* + \tilde{x}_a^*}{2}$. With x_a^* , the location \mathbf{x}_a can be calculated according to (48), so as \mathbf{x}_b . Therefore, three virtual TVs is enough for the SV to detect the position of the actual TV. This finishes the proof.

E. Proof of Proposition 4

Based on the line function (51), as well as the symmetric geometry relation between virtual TV ℓ and the actual one, it is easy to establish the mathematical relation between $\mathbf{x}^{(\ell)}$ and \mathbf{x} as

$$\begin{cases} x = x^{(\ell)} + \Delta x^{(\ell)} \\ z = z^{(\ell)} + \tan(\theta_\ell^*) \cdot \Delta x^{(\ell)} \end{cases}, \quad (64)$$

where $\Delta x^{(\ell)}$ is the x -direction projection of distance between (x, z) and $(x^{(\ell)}, z^{(\ell)})$. The middle point of (x, z) and $(x^{(\ell)}, z^{(\ell)})$ locates at the surface ℓ , meaning that the middle point $(x^{(\ell)} + \frac{\Delta x^{(\ell)}}{2}, z^{(\ell)} + \tan(\theta_\ell^*) \cdot \frac{\Delta x^{(\ell)}}{2})$ should satisfy function (51). Thus we have

$$z_a^{(\ell)} + z_a - \frac{1}{\tan(\theta_\ell^*)} (2x^{(\ell)} + \Delta x^{(\ell)} - x_a^{(\ell)} - x_a) = 2z^{(\ell)} + \tan(\theta_\ell^*) \cdot \Delta x^{(\ell)}. \quad (65)$$

The result derived from (65) is given as

$$\Delta x^{(\ell)} = \frac{\tan(\theta_\ell^*)}{1 + \tan^2(\theta_\ell^*)} \left(\frac{x_a^{(\ell)} + x_a^*}{\tan(\theta_\ell^*)} + z_a^{(\ell)} + z_a^* - \frac{2x^{(\ell)}}{\tan(\theta_\ell^*)} - 2z^{(\ell)} \right). \quad (66)$$

Bring (66) into (64), the result (52) can be obtained by replacing (x, z) with (x^*, z^*) .

REFERENCES

- [1] Z. Zhang, S. Ko, R. Wang, and K. Huang, "Millimeter-wave multi-point vehicular positioning for autonomous driving," in *GLOBECOM 2019 - 2019 IEEE Global Commun. Conf.*, Dec 2019, pp. 1–6.
- [2] H. Li, "Landscape detection by leveraging millimeter wave communication signals," in *ICC 2019 - 2019 IEEE Intl. Conf. on Commun. (ICC)*, May 2019, pp. 1–6.
- [3] S. Ko, H. Chae, K. Han, S. Lee, and K. Huang, "V2X-based vehicular positioning: Opportunities, challenges, and future directions," 2019. [Online]. Available: <http://arxiv.org/abs/1908.04606>
- [4] K. Liu, H. B. Lim, E. Frazzoli, H. Ji, and V. C. S. Lee, "Improving positioning accuracy using GPS pseudorange measurements for cooperative vehicular localization," *IEEE Trans. Veh. Technol.*, vol. 63, no. 6, pp. 2544–2556, July 2014.
- [5] F. Gustafsson and F. Gunnarsson, "Mobile positioning using wireless networks: possibilities and fundamental limitations based on available wireless network measurements," *IEEE Signal Process. Mag.*, vol. 22, no. 4, pp. 41–53, July 2005.
- [6] S. Zhu and Z. Ding, "Distributed cooperative localization of wireless sensor networks with convex hull constraint," *IEEE Trans. Wireless Commun.*, vol. 10, no. 7, pp. 2150–2161, 2011.
- [7] S. Gezici, G. B. Giannakis, H. Kobayashi, A. F. Molisch, H. V. Poor, and Z. Sahinoglu, "Localization via ultra-wideband radios: a look at positioning aspects for future sensor networks," *IEEE Signal Process. Mag.*, vol. 22, no. 4, pp. 70–84, July 2005.
- [8] J. Shen, A. F. Molisch, and J. Salmi, "Accurate passive location estimation using ToA measurements," *IEEE Trans. Wireless Commun.*, vol. 11, no. 6, pp. 2182–2192, June 2012.
- [9] K. Fujii, Y. Sakamoto, W. Wang, H. Arie, A. Schmitz, and S. Sugano, "Hyperbolic positioning with antenna arrays and multi-channel pseudolite for indoor localization," *Sensors*, vol. 15, no. 10, pp. 25 157–25 175, 2015.
- [10] K. Han, S. Ko, H. Chae, B. Kim, and K. Huang, "Hidden vehicle sensing via asynchronous V2V transmission: A multi-path-geometry approach," *IEEE Access*, vol. 7, pp. 169 399–169 416, 2019.
- [11] L. Yujiri, M. Shoucri, and P. Moffa, "Passive millimeter wave imaging," *IEEE Microw. Mag.*, vol. 4, no. 3, pp. 39–50, Sept 2003.
- [12] D. M. Sheen, D. L. McMakin, and T. E. Hall, "Three-dimensional millimeter-wave imaging for concealed weapon detection," *IEEE Trans. Microw. Theory Techn.*, vol. 49, no. 9, pp. 1581–1592, Sep 2001.
- [13] C. Nguyen and J. Park, *Stepped-Frequency Radar Sensors: Theory, Analysis and Design*. Springer Intl. Publishing, 2016.

- [14] S. S. Ahmed, A. Schiessl, F. Gumbmann, M. Tiebout, S. Methfessel, and L. Schmidt, "Advanced microwave imaging," *IEEE Microw. Mag.*, vol. 13, no. 6, pp. 26–43, Sept 2012.
- [15] X. Zhuge and A. G. Yarovoy, "Three-dimensional near-field MIMO array imaging using range migration techniques," *IEEE Trans. Image Process.*, vol. 21, no. 6, pp. 3026–3033, June 2012.
- [16] H. V. Duong, M. A. Lefsky, T. Ramond, and C. Weimer, "The electronically steerable flash lidar: A full waveform scanning system for topographic and ecosystem structure applications," *IEEE Trans. Geosci. Remote Sens.*, vol. 50, no. 11, pp. 4809–4820, Nov 2012.
- [17] R. H. Rasshofer, M. Spies, and H. Spies, "Influences of weather phenomena on automotive laser radar systems," *Advances in Radio Science*, vol. 9, pp. 49–60, 2011.
- [18] D. Maturana and S. Scherer, "VoxNet: A 3D convolutional neural network for real-time object recognition," in *2015 IEEE/RSJ Intl. Conf. Intell. Robots Syst. (IROS)*, Sep. 2015, pp. 922–928.
- [19] H. Zhao, R. Mayzus, S. Sun, M. Samimi, J. K. Schulz, Y. Azar, K. Wang, G. N. Wong, F. Gutierrez, and T. S. Rappaport, "28 GHz millimeter wave cellular communication measurements for reflection and penetration loss in and around buildings in new york city," in *2013 IEEE Intl. Conf. on Commun. (ICC)*, June 2013, pp. 5163–5167.
- [20] D. Cohen, Y. C. Eldar, and A. M. Haimovich, "Sub-Nyquist pulse doppler MIMO radar," in *2017 IEEE Intl. Conf. Acoust., Speech, Signal Process. (ICASSP)*, March 2017, pp. 3201–3205.
- [21] J. Li, X. Zhang, R. Cao, and M. Zhou, "Reduced-dimension MUSIC for angle and array gain-phase error estimation in bistatic mimo radar," *IEEE Commun. Letters*, vol. 17, no. 3, pp. 443–446, March 2013.
- [22] R. Schmidt, "Multiple emitter location and signal parameter estimation," *IEEE Trans. Antennas Propag.*, vol. 34, no. 3, pp. 276–280, 1986.
- [23] Q. Cheng, A. Alomainy, and Y. Hao, "Near-field millimeter-wave phased array imaging with compressive sensing," *IEEE Access*, vol. 5, pp. 18975–18986, 2017.
- [24] A. Goldsmith, *Wireless communications*. Cambridge: Cambridge University Press, 2005.
- [25] H. Guo, K. Low, and H. Nguyen, "Optimizing the localization of a wireless sensor network in real time based on a low-cost microcontroller," *IEEE Trans. Ind. Electron.*, vol. 58, no. 3, pp. 741–749, March 2011.
- [26] W. Mascarenhas, "The divergence of the BFGS and gauss newton methods." *Mathematical Programming*, vol. 147, no. 1/2, pp. 253 – 276.
- [27] M. Weib, "Synchronisation of bistatic radar systems," in *IGARSS 2004. 2004 IEEE Intl. Geosci. Remote Sens. Symp.*, vol. 3, Sep. 2004, pp. 1750–1753 vol.3.
- [28] Y. Wu, Q. Chaudhari, and E. Serpedin, "Clock synchronization of wireless sensor networks," *IEEE Signal Process. Mag.*, vol. 28, no. 1, pp. 124–138, Jan 2011.
- [29] O. K. Ersoy, *Diffraction, Fourier Optics and Imaging*. John Wiley & Sons, Ltd, 2006, ch. 4, pp. 41–62.
- [30] P. Davis, *Interpolation and Approximation*, ser. Dover Books on Mathematics. Dover Publications, 1975.
- [31] M. I. Skolnik, *Introduction to radar systems (2nd edition)*, 1980, vol. 1.
- [32] D. Barrick, "Rough surface scattering based on the specular point theory," *IEEE Trans. Antennas and Propag.*, vol. 16, no. 4, pp. 449–454, July 1968.
- [33] K. Sato, T. Manabe, T. Ihara, H. Saito, S. Ito, T. Tanaka, K. Sugai, N. Ohmi, Y. Murakami, M. Shibayama, Y. Konishi, and T. Kimura, "Measurements of reflection and transmission characteristics of interior structures of office building in the 60-GHz band," *IEEE Trans. Antennas Propag.*, vol. 45, no. 12, pp. 1783–1792, Dec 1997.
- [34] D. P. Huttenlocher, G. A. Klanderman, and W. J. Rucklidge, "Comparing images using the Hausdorff distance," *IEEE Trans. Pattern Anal. Mach. Intell.*, vol. 15, no. 9, pp. 850–863, Sep 1993.